THESIS

TRACKING THE TERRESTRIAL HYDROCLIMATE AND PALEOCLIMATE RESPONSE TO CHANGES IN ATMOSPHERIC pCO_2 USING STABLE OXYGEN AND CARBON ISOTOPES: A PROXY-MODEL COMPARISON ACROSS CENOZOIC EURASIA

Submitted by

Elizabeth Driscoll

Department of Geosciences

In partial fulfillment of the requirements

For the Degree of Master of Science

Colorado State University

Fort Collins, Colorado

Fall 2022

Master's Committee:

Advisor: Jeremy Caves Rugenstein

Scott Denning
Patrick Keys
Michael Ronayne

ABSTRACT

TRACKING THE TERRESTRIAL HYDROCLIMATE AND PALEOCLIMATE RESPONSE TO CHANGES IN ATMOSPHERIC pCO_2 USING STABLE OXYGEN AND CARBON ISOTOPES: A PROXY-MODEL COMPARISON ACROSS CENOZOIC EURASIA

Despite well-known constraints on the global hydrologic cycle with future warming, the response of the terrestrial hydrologic cycle – and hence future available freshwater resources – remains uncertain. This is largely due to the difficulty in predicting changes in environmental parameters such as precipitation (P), evapotranspiration (ET), and runoff (q). Shifts in the ratio of P/ET can be quantified using the $\delta^{18}O$ of precipitation ($\delta^{18}O_p$), given that P decreases $\delta^{18}O_p$ and ET increases $\delta^{18}O_p$. Additionally, the $\delta^{13}C$ composition of soil can provide insight into shifts in P and ET by recording the response of vegetation to changing climate.

To better understand how the terrestrial water cycle will change with future warming, we utilize the geologic stable oxygen and carbon ($\delta^{18}O$ and $\delta^{13}C$) isotope record to reconstruct past spatial distribution and longitudinal gradients of $\delta^{18}O_p$ and $\delta^{13}C$ across Eurasia during periods of high atmospheric pCO_2. We compile nearly 15,000 samples of authigenic carbonate and tooth enamel samples that span the Cenozoic Era across Eurasia. Oxygen isotopes in these proxies record the meteoric water $\delta^{18}O$ signature during the time of mineral formation, which allows for reconstruction of moisture transport in the past. Soil carbonate $\delta^{13}C$, in turn, captures shifts in primary productivity and aridity, providing a complementary viewpoint to changes in the hydroclimate response to increased atmospheric pCO_2.

The $\delta^{18}O$ record indicates that the westerlies have driven moisture transport across Eurasia since at least the Eocene. Additionally, steeper $\delta^{18}O_p$ gradients correspond with periods of high pCO_2, suggesting a relatively high P/ET ratio and/or a higher evaporative fraction of ET, which preferentially supplies air parcels with ^{18}O and thus steepens the gradient. The $\delta^{13}C$ record demonstrates an increase in aridity in Asia during the late Cenozoic concurrent with stable (or slightly increased) primary productivity in Europe. Both isotopic records indicate that hydroclimate is driven predominantly by shifts in global climate due to changes in pCO_2 and is only marginally impacted by dramatic changes in Cenozoic paleogeography.

The proxy $\delta^{18}O_p$ gradients were compared to $\delta^{18}O_p$ gradients produced by both a simple reactive transport model and by an isotope-enabled earth system model. Gradients of $\delta^{18}O_p$ produced by both models under varying pCO_2 demonstrate a mismatch between the proxy and model $\delta^{18}O$ gradient response to CO_2 – both models generate shallow gradients during periods of high pCO_2 (4x Pre-Industrial pCO_2) and generate the steepest gradients with the lowest pCO_2 (Pre-Industrial pCO_2). The proxy-model mismatch implies that these models may be misrepresenting the response of transpiration or the partitioning of P into ET and q at higher atmospheric CO_2 concentrations.

ACKNOWLEDGMENTS

First and foremost, I would like to thank my advisor, Dr. Jeremy Rugenstein, for his guidance throughout this project. I am very grateful to have been his student and one of the founding members of the GeoPAST research group at CSU! I truly appreciate his enthusiasm throughout the project and my graduate experience in general. Thank you to my committee members, Dr. Scott Denning, Dr. Pat Keys, and Dr. Mike Ronayne, for their many helpful conversations and support throughout the analysis and writing process.

I gratefully acknowledge the assistance from Michael Needham for processing the CESM output, running the iCESM, and for all the time he spent helping me interpret the modeling results for this project – his work was invaluable! I also want to thank Tyler Kukla for his help running the reactive transport model and interpreting the results, as well as for having many helpful conversations with me. I would also like to thank Dr. Pat Keys for his help with generating the results from the WAM and for his help in interpreting the results.

Lastly, thank you to my family, friends, partner, and fellow graduate students for all their support along the way!

TABLE OF CONTENTS

LIST OF TABLES

LIST OF FIGURES

Introduction

The response of the terrestrial water cycle to higher atmospheric CO_2 remains unclear but has important implications for future freshwater resources in a warmer climate. However, it is difficult to constrain the response of the terrestrial hydrological cycle to warming because this cycle is defined by several interacting components including precipitation (P), evapotranspiration (ET), and runoff (q), each of which may change independently with warming (Pendergrass and Hartmann, 2014; Scheff and Friarson, 2014; Scheff et al., 2017). Some components of the water cycle are well constrained under projections of higher atmospheric CO_2. For example, global mean precipitation (and hence global mean evaporation due to mass balance constraints) scale with the Earth's energy budget and have a sensitivity of ~2%/°C (Held and Soden, 2006; Stephens and Hu, 2010; Pendergrass and Hartmann, 2014). In contrast, saturation vapor pressure should increase by 7%/°C of warming, per the Clausius-Clapeyron relation, increasing the specific humidity of the atmosphere. Though globally P must equal evaporation (E), spatial differences in P-E will be amplified in a warmer climate, largely following the 'wet-gets-wetter, dry-gets-drier' paradigm (particularly over the ocean) as a result of this increase in atmospheric water vapor and moisture transport in a warmer climate (Held and Soden, 2006; Seager et al., 2010).

However, the terrestrial responses of P, E, and ET to warming are more uncertain. This uncertainty arises because the land surface plays a critical role in modifying the hydrological cycle (Milly and Dunne, 1994). The land surface, unlike over the ocean, is not well-watered, meaning that ET is subject to both energetic and mass balance constraints. Additionally, much of the terrestrial hydrological cycle is mediated by plants, which use water (*i.e.,* transpiration, T) to fix carbon. Although higher CO_2 may fertilize plants, spurring increased productivity, plant growth

may be limited by other nutrient or water constraints at higher CO_2. The response of E from soils and T from plants to a higher CO_2 world will determine the partitioning of P to ET and to q (Greve et al., 2014; Milly and Dunne, 2016; Scheff et al., 2017). Though precipitation is likely to increase at high-latitudes, changes in the mid-latitudes and tropics are dominated by regional changes of varying sign (Greve et al., 2014; Scheff et al., 2017). Thus, predicting the response of the terrestrial hydrological cycle to warming remains unresolved and difficult to constrain with climate models (Findell et al. 2019).

To improve our understanding of the long-term terrestrial hydrologic cycle to warming, we use the paleoclimate record to evaluate how these critical parameters – P, ET, and q – will change as CO_2 rises. We focus on periods of extended warmth and high CO_2 during the Cenozoic, which is characterized by a global flora regime similar to the modern, dominated by angiosperms. To constrain past hydroclimate, we use the stable isotopes of oxygen and carbon as preserved in authigenic materials, such as calcium carbonate or tooth enamel. Oxygen isotopes ($\delta^{18}O$) are tracers of the hydrological cycle and are particularly sensitive to the relationship between P and ET. As moisture is transported over a continent, P preferentially removes ^{18}O from water vapor, whereas ET tends to resupply the atmosphere with ^{18}O. Consequently, the rate of $\delta^{18}O$ decrease across a continent reflects – to first-order – the ratio of P and ET (and thus q) along a prevailing storm track. This isotopic depletion of a single airmass across a continent can be quantified through a longitudinal isotopic gradient, which is sensitive to many hydroclimate parameters including the fraction of transpiration in evapotranspiration, amount of precipitable water, air temperature, and relative humidity. These gradients are particularly useful when studying different geologic periods because they are not sensitive to changes in the $\delta^{18}O$ of the moisture source. In turn, carbon isotopes ($\delta^{13}C$) preserved in pedogenic materials (minerals forming in soil) incorporate carbon that

reflects the dominant regional vegetation type (C3 vs. C4), atmospheric pCO_2, and the concentration of soil-respired CO_2, which reflects overlying plant productivity (Cerling, 1984).

Several processes can modify the rainout (and hence $\delta^{18}O$) of moisture across land and modify the fractionation of $\delta^{18}O$ between meteoric water and authigenic carbonate. Spatial compilations of stable isotopes in the geologic record can be used to distinguish between the competing effects on the $\delta^{18}O$ of water that result from changes in climate, topography, and moisture sources, which are otherwise difficult to disentangle from a single sedimentary section. For example, temperature-dependent fractionation of oxygen isotopes has resulted in use of these proxies to reconstruct past climate change (Baker et al., 2019; Burgener et al., 2019; Lachniet, 2009; Methner et al., 2020), and the known effect of increased air parcel rainout with higher topography is often utilized to constrain paleotopographic changes (Rowley and Garzione, 2007; Poage and Chamberlain, 2001; Krsnik et al., 2021; Garzione et al., 2004). Further, mixing of air masses with different isotopic compositions can also result in changing the $\delta^{18}O$ recorded in authigenic materials (Caves et al., 2015; Huyghe et al., 2018). These competing effects can be distinguished and quantified using large-scale maps of isotopic distribution which allow attribution of shifts in $\delta^{18}O$ to either local or global influences (Caves et al., 2015; Caves et al., 2016; Rugenstein and Chamberlain, 2018; Liu et al., 2010; Mix et al., 2011). Maps of $\delta^{13}C$ can be similarly utilized to assign shifts in carbon isotopes to changing atmospheric pCO_2, shifts in vegetation regimes between C3 and C4 vegetation, and changes in soil respiration fluxes related to primary productivity and mean annual precipitation (Caves et al., 2016; Rugenstein and Chamberlain, 2018).

We use isotope maps and longitudinal gradients and profiles of $\delta^{18}O$ and $\delta^{13}C$ across the Eurasian continent through the Cenozoic Era to investigate the response of terrestrial hydroclimate

and vegetation to warm periods, characterized by high atmospheric pCO_2, to understand potential responses to future warming. Eurasia provides a particularly favorable study region as it is the largest continental area on Earth and is largely dominated by a single air mass, with moisture flux from Europe to Asia driven by the westerlies. Because much of the precipitation that falls over Asia is sourced from evaporated continental moisture from Europe, one can isolate the effects of higher pCO_2 on the terrestrial water cycle and the role of the land surface in driving changes in hydroclimate by largely eliminating influence from marine moisture sources. We additionally compare the results of the proxy-generated $\delta^{18}O$ longitudinal gradients to gradients produced by a simple reactive transport model and by an isotope-enabled earth system model. The proxy $\delta^{18}O$ and $\delta^{13}C$ results suggest that the westerlies have driven moisture transport across Eurasia since at least the Eocene, and that changes in moisture transport and in vegetation over the Cenozoic are driven largely by the decline in atmospheric pCO_2 over this period, rather than by the dramatic changes in paleogeography. Furthermore, we find that the steepest proxy $\delta^{18}O$ gradients correlate with periods of high pCO_2, and the shallowest proxy gradients occur late in the Cenozoic during times of low pCO_2. Additionally, we find that neither the reactive transport model nor the earth system model capture the response of steeper gradients with high pCO_2, which implies that models may misrepresent changes in plant physiology or the partitioning of P into ET and q in response to higher pCO_2.

Background

i. Oxygen and Carbon Isotope Systematics

a. Oxygen

The isotopic composition of precipitation is sensitive to many processes, including changes in temperature, the effect of atmospheric circulation patterns on moisture transport, and sources of atmospheric vapor (Rozanski et al., 1992; Rozanski et al., 1993; Liu et al., 2010). As an air mass travels inland, the oxygen isotopes in precipitation ($\delta^{18}O_p$) decrease along dominant circulation trajectories with increased distance from the ocean (Rozanski et al., 1993; Winnick et al., 2014; Liu et al., 2010). Along a storm track, this removal of ^{18}O during condensation is described by Rayleigh distillation. Similarly, decreases in surface temperature result in a decrease in $\delta^{18}O_p$ (Rozanski et al., 1992). Air masses that converge on a given location from different circulation trajectories both may have 1) different initial isotopic compositions and 2) experienced varying degrees of rainout, generating distinct $\delta^{18}O_p$ compositions from these independent moisture sources (Sjostrom and Welker, 2009; Aggarwal et al., 2012; Liu et al., 2010). The mixing of two air masses generates an intermediate isotopic signal between the $\delta^{18}O$ of the two parcels at the point of convergence.

Although the degree of rainout is the main control on longitudinal $\delta^{18}O_p$ gradients along a single storm track, Rayleigh distillation alone doesn't account for spatial patterns of oxygen isotopes in precipitation (Winnick et al., 2014; McDermott et al., 2011; Rugenstein and Chamberlain, 2018). The recycling of moisture from the land surface through ET allows air parcels to be resupplied with either fractionated $\delta^{18}O$ from E, which preferentially returns ^{16}O to the atmosphere, or approximately unfractionated $\delta^{18}O$ through plant T, which resupplies air parcels

with ^{18}O (Numaguti, 1999; Kurita et al., 2004). Thus, continental moisture recycling is dependent on both climatic influences and land surface conditions, such as vegetation and soil moisture (Findell et al., 2019). Because transpiration is estimated to comprise much of the ET flux (~64%; Good et al., 2015) on a global level, the $\delta^{18}O_p$ along a storm track will be higher than that predicted by pure Rayleigh distillation due to this input of ^{18}O back into the atmosphere.

Topography imparts a substantial effect on $\delta^{18}O$ by forcing more rainout in a short distance; as air parcels ascend over topography, they become systematically depleted in ^{18}O (Rowley et al., 2001; Rowley and Garzione, 2007; Rozanski et al., 1993). Paleoaltimetry studies frequently exploit the relationship between elevation and $\delta^{18}O$ to reconstruct the elevation of ranges at the time of carbonate formation – thus, these studies are a specific application of fact that $\delta^{18}O$ along a storm track is set by the degree of rainout vs. ET, with orography forcing more rainout over a short distance (Mix et al., 2011; San Jose et al., 2020). However, applying stable isotope paleoaltimetry to past climates implicitly assumes that the hydroclimate parameters that control $\delta^{18}O_p$ were the same in the past as in the present (Botsyun et al., 2019), which may result in erroneous interpretations. Using pre-determined theoretical or empirical isotopic lapse rates can produce uncertainties in paleoelevation estimates given the high degree of sensitivity of $\delta^{18}O_p$, and thus the $\delta^{18}O_p$-elevation gradient, to regional or global climate change, or to changes in atmospheric circulation patterns caused by topographic deflection of air masses (Huyghe et al., 2018; Botsyun et al., 2019). Additionally, uplift of a range may induce hydroclimate changes by increasing runoff partitioning and decreasing recycling of moisture through ET (Kukla et al., 2019; Rugenstein and Chamberlain, 2018), further modifying downwind $\delta^{18}O_p$.

The isotopic composition of past meteoric water is recorded in a variety of authigenic materials, including pedogenic (soil) carbonates, lacustrine (lake) carbonates, and speleothem

(cave) carbonates (Breecker et al., 2009; Leng and Marshall, 2004; McDermott et al., 2011; Lachniet, 2009). Carbonate that forms in lake or soil water is generally thought to be in isotopic equilibrium with the water in which it forms; thus, the $\delta^{18}O$ of meteoric water ($\delta^{18}O_{mw}$) is related to the $\delta^{18}O$ of carbonate ($\delta^{18}O_c$) through a temperature-dependent fractionation (Rugenstein and Chamberlain, 2018; Kim and O'Neil, 1997). To reconstruct $\delta^{18}O_{mw}$ from the $\delta^{18}O_c$ of proxy materials, approximations of the temperature of mineral formation must be used to convert between the two values, which may result in inexact $\delta^{18}O_p$ estimates (Burgener et al., 2019). However, because the fractionation of $\delta^{18}O$ between water and calcite varies by only approximately -0.2‰/°C at surface temperatures, an error of many degrees would be required to considerably outweigh the much more dominant signal of atmospheric processes on $\delta^{18}O_p$ (Kim and O'Neil, 1997; Rugenstein and Chamberlain, 2018).

Similarly, the phosphate and carbonate components of tooth enamel reliably record the $\delta^{18}O$ of the animal's primary water source (Kohn and Law, 2006). Local isotope signals are recorded in bioapatite, a primary component of tooth enamel, through ingestion of organic material and surface water (Fricke et al., 2009). $\delta^{18}O$ is preserved in bioapatite both in a carbonate and phosphate component; although the phosphate component is thought to be the most resistant to post-mineralization alteration, the carbonate component still retains high preservation potential (Kohn, 1996). The $\delta^{18}O$ of tooth enamel ($\delta^{18}O_e$) represents the $\delta^{18}O$ of body water ($\delta^{18}O_{bw}$), which itself reflects oxygen uptake (e.g., breath O_2 and H_2O, drinking and consuming water) and loss (e.g., breath CO_2 and H_2O, water in urine and waste, transcutaneous water loss) during tooth development (Kohn, 1996; Matson and Fox, 2010; Domingo et al., 2013). Reconstructions of $\delta^{18}O_{mw}$ from mammal $\delta^{18}O_e$ offer different complications from that of $\delta^{18}O_c$ – although the internal regulation of body temperature alleviates uncertainty of mineral formation temperature by

generating a constant offset of $\delta^{18}O_{bw}$ and $\delta^{18}O_e$ of ~18‰, physiological factors (particularly related to animal size) affect $\delta^{18}O_{bw}$ by altering the magnitude of inward and outward oxygen fluxes (Koch, 2007; Matson and Fox, 2010; Domingo et al., 2013). Due to these physiological differences, various taxa-specific conversions from $\delta^{18}O_e$ to $\delta^{18}O_{mw}$ have been established for modern mammals, and estimates of paleo-$\delta^{18}O_{mw}$ rely on comparison to the closest living relative of the fossil taxa (Domingo et al., 2013).

Secondary influences on $\delta^{18}O$ of carbonate or enamel ($\delta^{18}O_{c/e}$) include evaporation, seasonality of isotopes in precipitation, and seasonality of carbonate formation. Evaporation, which may occur in lakes and the upper 30-50 cm of soil profiles (Leng and Marshall, 2004; Breecker et al., 2009), leads to enrichment in the $\delta^{18}O$ of the residual water. This can drive $\delta^{18}O_c$ towards more positive isotopic values relative to local precipitation. Although sampling pedogenic carbonates below 50 cm may reduce evaporative effects, $\delta^{18}O_c$ below this depth is affected by seasonality. Precipitation $\delta^{18}O$—particularly in mid- and high-latitudes—has stark seasonal patterns due to differences in ET and total precipitable water that co-vary with the season. In the summertime, ET rates and total precipitable water are high, resulting in recycling of moisture back into the atmosphere and elevated $\delta^{18}O_p$ (Kurita et al., 2004). During cooler seasons, continental ET rates are small and total precipitable water is low, and thus $\delta^{18}O_p$ more closely resembles pure Rayleigh distillation, generating more negative $\delta^{18}O_p$ values in the winter than summer and producing steeper isotopic longitudinal gradients. Seasonal variations in $\delta^{18}O_p$ are dampened in large meteoric water reservoirs, such as large, hydrologically open lakes and rivers (Leng and Marshall, 2004). Carbonate formation itself may also be seasonally biased; Breecker et al. (2009) suggest that pedogenic carbonate forms when the soil is warm, dry, and has low soil pCO_2. Speleothems, conversely, are thought to record wintertime $\delta^{18}O$ signals (James et al., 2015).

These competing effects make it difficult to attribute changes in $\delta^{18}O$ to changes in temperature, net rainout, topography, or in the dominant moisture source that reflect shifts in atmospheric circulation when examining data from a single stratigraphic section or a limited region. For example, if carbonates in single basin record a decrease in $\delta^{18}O$ over several Ma, such a decrease could be attributed to 1) an increase in regional or global temperature, 2) an increase in upwind elevation or elevation in the basin itself, 3) changes in upwind vegetation resulting in a lower transpiration fraction of ET, 4) changes in moisture source(s), with the new signal being dominated by an air parcel that has a lower initial $\delta^{18}O$ or has experienced greater rainout, or 5) biases in the $\delta^{18}O$ preserved in the proxy material, such as evaporative effects or seasonality. Spatial datasets of $\delta^{18}O_p$ can alleviate some of these uncertainties by reconstructing pathways of inland moisture transport using the continental-scale spatial distribution of $\delta^{18}O$ (Caves et al., 2015; McDermott et al., 2011; Rugenstein and Chamberlain, 2018; Mix et al., 2011; Liu et al., 2010; Li and Garzione, 2017).

b. Carbon

The factors that modify $\delta^{13}C$ in authigenic minerals are distinct from that of $\delta^{18}O$. Paleosol carbonate is thought to form in equilibrium with soil CO_2 due to the slow precipitation of carbonate and because changes in the soil itself (below 30 cm) occur slowly (Breecker et al., 2010). Thus, these carbonates provide a record of soil $\delta^{13}C$ at the time of formation. The $\delta^{13}C$ of soil carbonates ($\delta^{13}C_c$) is driven primarily by the concentration and $\delta^{13}C$ of atmospheric CO_2 and soil-respired CO_2 and, following the expansion of C4 vegetation during the Miocene, by differences in C3 vs. C4 vegetation cover (Cerling, 1991; 1984). The CO_2 required to precipitate pedogenic carbonate is derived from root respiration and microbial oxidation of organic matter in the soil (which combined equate to soil respiration), and from diffusion of atmospheric CO_2 into the soil

(Ehleringer et al., 2000; Breecker et al., 2009; Abels et al., 2016). Biogenically produced CO_2 in the soil mixes with atmospheric CO_2, with the net increase in soil CO_2 concentrations resulting in diffusion of CO_2 into the atmosphere (Breecker et al., 2009). The rate of the CO_2 flux between the soil and atmosphere is influenced by properties such as the strength of the soil-atmosphere CO_2 gradient, air temperature, and wind speed (Raich and Schlesinger, 1992). The resulting soil CO_2 $\delta^{13}C$ reflects the relative abundance of atmospheric CO_2 and its $\delta^{13}C$, the production of CO_2 within the soil via respiration, and the $\delta^{13}C$ of the soil respiration flux (Cerling, 1984; Breecker et al., 2009). The $\delta^{13}C$ of soil is always less than $\delta^{13}C$ of atmospheric CO_2, and therefore, increasing contribution of atmospheric CO_2 will lead to an increase in $\delta^{13}C_c$, and vice versa.

The soil respiration flux of $\delta^{13}C$ is largely driven by plant fractionation processes, which vary between C3 and C4 vegetation types. During photosynthesis, plants discriminate against the heavier ^{13}C, with the different photosynthetic pathways in C3 vs. C4 plants resulting in distinct isotopic values (O'Leary, 1988). The photosynthetic fractionation of $\delta^{13}C$ in C4 vegetation is small, resulting in high $\delta^{13}C$ values of ~-14‰ (O'Leary, 1988; Ehleringer et al., 2000). This fractionation is much greater in C3 vegetation, resulting in lower $\delta^{13}C$ values of ~-28‰ (O'Leary, 1988; Ehleringer et al., 2000). These varying fractionations between different plant types induce changes in the $\delta^{13}C$ of pedogenic carbonates by significantly altering the $\delta^{13}C$ of the soil.

Aridity alone alters the fractionation of $\delta^{13}C$ in C3 plants; field studies find that the fractionation of carbon isotopes during CO_2 uptake and fixation by the leaf monotonically increases with increased mean annual precipitation (MAP) and thus mirrors trends in gross primary productivity (Diefendorf et al., 2010; Kohn, 2010; Bond-Lamberty and Thompson, 2010). Increased primary productivity and MAP results in higher soil respiration flux and thus lower $\delta^{13}C_c$, whereas lower MAP forces plants to reduce discrimination against the ^{13}C isotope, driving

higher $\delta^{13}C_c$ values. Thus, anomalously high $\delta^{13}C_c$, prior to the onset of C4 dominance or in locations with low C4 abundance, indicates arid conditions. The effect of aridity on C3 plant $\delta^{13}C$ is substantial, with such plants in regions that experience high MAP (*i.e.,* the understory of closed-canopy forests) having an average $\delta^{13}C$ of -31.5‰, while C3 plants in extremely arid regions (MAP < 10 mm/yr) having $\delta^{13}C$ as high as -23‰ (Kohn, 2010).

Although carbon isotope values recorded in soil carbonates are commonly used as a proxy to reconstruct past atmospheric pCO_2 or the spread of C4 vegetation, their sensitivity to soil respiration means they may also be used to reconstruct past soil respiration fluxes (Caves et al., 2016; Rugenstein and Chamberlain, 2018). In general, lower $\delta^{13}C_c$ values correspond with high concentrations of soil CO_2, and thus high soil respiration flux (Cerling, 1984; Caves et al., 2016). Soil respiration fluxes, in turn, correlate with plant productivity (Raisch and Schlesinger 1992). Because lower MAP also decreases the depth of carbonate formation, and $\delta^{13}C$ decreases with depth in the soil, these conditions (aridity and shallow formation) both tend to increase $\delta^{13}C_c$ (Cerling, 1984; Breecker et al., 2009). Therefore, higher $\delta^{13}C_c$ reflects aridity through reduced soil respiration fluxes, higher $\delta^{13}C$ of soil organic matter due to reduced fractionation of carbon isotopes with lower MAP, and/or lower depth of carbonate formation.

ii. Modern Eurasian Hydroclimate

Western and Eastern Eurasia are linked via moisture transport along the mid-latitude westerlies. Westerly-sourced moisture is the dominant moisture flux between Europe and Asia, with continental moisture recycled from Europe as the major source of moisture for precipitation that falls over Asia (van der Ent et al., 2010; Wypych et al., 2018; Bisselink and Dolman, 2008; Wang et al., 2017). Generally, Europe acts as a source for atmospheric moisture, with 40-70% of evaporated moisture in Europe returning as precipitation to a continental area, except for regions

of high elevation that drive orographic rainout such as the Alps and Caucuses (Benedict et al., 2021; Bisselink and Dolman, 2008). Central Eurasia is a major sink region for continental precipitation that originated further west in Eurasia, with much of that precipitation eventually returning to the atmosphere via ET and reprecipitating over eastern Eurasia (Bisselink and Dolman, 2008; van der Ent et al., 2010; Wang et al., 2017). The majority of moisture recycling over the Eurasian continent occurs during the summer; overall net atmospheric water transport is from the oceans to inland during the winter, and from inland to the oceans during the summer (Numaguti, 1999). In the winter, most water in precipitation is derived from the oceans – water from the North Atlantic intrudes farther than other oceanic sources due to the strong westerly flow in the mid- to high latitudes (Sodemann and Zubler, 2010; Numaguti, 1999). The direct contribution of oceanic moisture in the summer becomes proportionately smaller as the amount of water evaporation from the land surface increases, with over 80% of precipitated water over Eurasia estimated as being supplied by terrestrial evaporation (Numaguti, 1999).

Despite these linkages, Europe and Asia have somewhat different climatic controls. On the western side of Eurasia, the Gulf Stream and North Atlantic Current control modern climate conditions (Utescher et al., 2015; Batibeniz et al., 2020). The North Atlantic Oscillation (NAO), a meridional oscillation in atmospheric mass which consists of the difference in atmospheric sea level pressure between the Azores High and Icelandic Low pressure fields, is linked to variations in the location and intensity of the surface westerlies from the Atlantic into Europe (Hurrell and van Loon, 1997; Tsanis and Tapoglou, 2019; Brittingham et al., 2019; Varlam et al., 2020). Much of the Northern Hemisphere's multidecadal climate variability is driven by the NAO (Tsanis and Tapoglou, 2019; Ruprecht et al., 2002). European climate exhibits distinct seasonality: the NAO drives winter climate variability, whereas local moisture recycling becomes more dominant in the

summer when zonal moisture transport is diminished (Zveryaev et al., 2008). The Mediterranean region is a climatic transition zone, situated between the dry subtropics and more humid Central and Northern European mid-latitude climates (Celle-Jeanton et al., 2001; Barcikowska et al., 2018). Precipitation in the northern Mediterranean is controlled by the NAO, while precipitation in the southern part is controlled by the descending branch of the Hadley Cell and cold surface water of the Canary Current (Hurrell and van Loon, 1997; Barcikowska et al., 2018).

Asia currently has wet monsoonal regions to the south and east of the Tibetan Plateau and has arid continental regions to the north and west of the plateau (>35°N) (Ao et al., 2021; Cheng et al., 2021). This arid region is dominated by the westerlies and lies beyond the reach of summer monsoonal moisture (Ao et al., 2021). The meteorological regime in Asia is influenced by five air masses: 1) polar air from the arctic, 2) continental recycled moisture from central Asia, 3) tropical air mass originating in the northern Pacific, 4) equatorial air mass from the western equatorial Pacific, and 5) equatorial air mass from the Indian Ocean (Araguás-Araguás et al., 1998). The dominance of these air masses is seasonally modulated by monsoonal activity and the seasonal displacement of the Intertropical Convergence Zone (Araguás-Araguás et al., 1998). Climate on the eastern side of Eurasia is closely linked to the East Asian Monsoon System, although climate in this region is complicated by the high topography (Utescher et al., 2015); the Tibetan Plateau acts as a strong delineator of climate regimes in Asia and separates the Indian Monsoon from the mid-latitude westerlies (Araguás-Araguás et al., 1998; Ao et al., 2021).

Due to the influence of topography and varying moisture sources in both Europe and Asia, the linkage in moisture transport across the continent via the westerlies is strongly dependent on latitude. Areas to the south largely receive moisture from non-westerly sources – the Mediterranean is a significant moisture source for southern Europe, and the Asian Monsoon for

much of southeast Asia (Numaguti, 1999; van der Ent et al., 2010). Central and northern regions in Eurasia are dominated by Atlantic moisture in western Eurasia, then by continental ET sourced from westerly upwind locations, particularly in the summertime (Numaguti, 1999; van der Ent et al., 2010). Thus, it is critical to identify the predominant moisture source for each region to study non-mixed westerly moisture transport across Eurasia.

iii. Moisture Source Tracking

We utilize HYSPLIT (the Hybrid Single-Particle LaGrangian Integrated Trajectory Model) to estimate contributions of moisture sources other than westerly/Atlantic (e.g., the Mediterranean Sea) to sites located in Eurasia (Stein et al., 2015; Rolph et al., 2017). HYSPLIT computes air parcel trajectories, allowing them to be tracked backward in time and space from a given location. Since $\delta^{18}O_p$ is affected by the degree of rainout along a storm track and by air mass mixing, HYSPLIT is used to understand how circulation and topography interact to modify moisture transport pathways. Air parcel trajectories were backtracked from a gridded set of locations (n=63) across a latitudinal range of 40°N to 55°N and longitudinal range of 0°E to 100°E. We find that North Atlantic moisture is the dominant (>50%) moisture source for all latitudes (40°N-55°N) from 0°E until 10°E, after which the Atlantic moisture only dominates at and above 50°N (Fig. A1). Mediterranean Sea moisture prevails at 40-45°N between 10-40°E (Fig. A1). The Black Sea, Baltic Sea, and Caspian Sea all have a local influence on nearby locations, usually contributing ≤50% of the moisture at locations within a 10° radius from the sites (Fig. A1). Finally, beyond 40°E, recycled continental moisture dominates the signal, with recycled moisture becoming dominant among all latitudes between 40-60°E, with northern sites exhibiting mostly recycled moisture less far inland (closer to the Atlantic) than southern sites that receive moisture from the smaller, regional moisture sources of the Mediterranean/Black/Baltic/Caspian Seas. Based on

these HYSPLIT results, we estimate that a westerly-dominated signal lies above 47°N in Europe and above 35°N in Asia, with the southern limit of mid-Eurasian westerly moisture falling between those (Fig. 1; Fig. A1).

Because HYSPLIT only tracks air parcels, and does not specifically track moisture pathways, we utilize the Eulerian moisture tracking scheme of the Water Accounting Model-2layers (hereafter WAM) of van der Ent et al. (2010; 2013) to ensure that the HYSPLIT results are accurately capturing movement of moisture across Eurasia. The WAM identifies the source region for precipitation that falls over a given location using a backtracking feature, allowing for identification of the specific upwind location from where the moisture evaporated (*i.e.,* the precipitationshed). For each grid cell and corresponding air column, the WAM accounts for incoming moisture from upwind evaporation and adjacent grid cells, moisture mixing within the column, and moisture exiting via precipitation using ERA-Interim Reanalysis data during the period of 1979-2014 (Keys et al., 2012; Dee et al., 2011). The WAM uses 6-hourly data for horizontal and vertical wind, surface pressure, and humidity, and 3-hourly data for precipitation and evaporation. We direct the reader to Keys and Wang-Erlandsson (2018) and Keys et al. (2018) for further details on the WAM. The WAM was run at three sites (3° x 3° domain) at which HYSPLIT had previously been run. Based upon the close match of precipitationsheds generated from HYSPLIT and the WAM at the same locations (Fig. A2), we conclude that HYSPLIT effectively captures moisture transport pathways and can be utilized to estimate contributions of moisture sources to various regions in Eurasia.

Methods

i. Compilation of Proxy Data

We compiled a database of authigenic mineral stable isotopes ($\delta^{18}O$ and $\delta^{13}C$) from a variety of geologic proxy materials across Eurasia that spans the Cenozoic Era (66 to 0 Ma). Coupled with a reactive transport model that simulates $\delta^{18}O_p$, we use this database to distinguish how moisture transport has evolved across Eurasia through geologic time. The paleo-data compilation includes 143 total publications, with 57 of these publications based on samples collected in Europe and 86 from Asia and totals 14,810 unique samples. The portion of the database that covers Asia was originally compiled by and discussed in Rugenstein and Chamberlain (2018). This compilation is under review for publication (Kukla et al., in review) and publicly available on the PATCH Lab website (Kukla et al., 2022a). Although the compilation includes a few samples from the Paleocene epoch, the subsequent discussion only examines data through the Eocene, as the spatial distribution of compiled Paleocene data is extremely limited.

The compilation predominantly includes stable isotope data from calcite proxies and tooth enamel phosphate, including paleosol carbonate nodules, lacustrine carbonates, speleothem carbonate, and mammal enamel from a diverse suite of taxa. Herein, we restrict the discussion of $\delta^{13}C$ exclusively to paleosol carbonate $\delta^{13}C$ as we are interested in using these values to track variations in productivity and plant communities across Eurasia; the discussion of $\delta^{18}O$ is not limited to any specific proxy. Isotopic data from each study was carefully reviewed for indications of evaporative enrichment or diagenetic alteration. Lacustrine datasets with positive covariation of carbon and oxygen isotopes were presumed to be evaporatively enriched, and thus only the lowest 20% of values were used in site-averages from those studies (Rowley and Currie, 2006; Cyr et al.,

2005; Li et al., 2015). Studies that indicated potential diagenetic influence were not included. Although mammal dentine and bone are also often reported in the literature, only mammal enamel was used in the $\delta^{18}O$ reconstructions, as it is the most resistant to alteration (Kohn, 1996). Enamel $\delta^{18}O$ from a range of large mammals was used to best ameliorate varying sensitivities of different animals to water composition and humidity (Kohn, 1996).

We also compiled modern meteoric water $\delta^{18}O$ data across Eurasia, including precipitation, river and stream water, and tap water $\delta^{18}O$ from the International Atomic Energy Agency's Global Network of Isotopes in Precipitation/Rivers (IAEA GNIP/GNIR) database and the Waterisotopes Database (IAEA/WMO, 2020; IAEA, 2020; Waterisotopes, 2020), as well as from a few individually reported studies (see compilation references, S1). Over 64,000 observations of modern $\delta^{18}O$ at 5,550 sites were compiled, with the earliest collection date in 1961.

ii. Conversion of proxy $\delta^{18}O$ to meteoric water $\delta^{18}O$

To directly compare the $\delta^{18}O$ between each of the geologic proxy types, the proxy $\delta^{18}O$ values were converted to the $\delta^{18}O$ of the water from which they precipitated. For carbonate $\delta^{18}O$ ($\delta^{18}O_c$), we interpolated modern surface air temperatures for each proxy sample location (Kanamitsu et al., 2002) and adjusted for estimated temperature differences in the past (relative to the modern) using Cenozoic temperature estimates from benthic foraminifera (Lear et al., 2000). We then used these estimated surface temperatures to calculate the ^{18}O fractionation between water and calcite using the fractionation factors of Kim and O'Neil ($10001n\alpha(\text{Calcite-}H_2O) = 18.03(103T^{-1}) - 32.42$; 1997) and reconstructed past meteoric water $\delta^{18}O$. For tooth enamel $\delta^{18}O$ ($\delta^{18}O_e$), we used previously published mammal-specific $\delta^{18}O_e - \delta^{18}O_w$ equations where possible. If no equation existed for a specific species, then a general equation calibrated for all mammals

was used (Amiot et al., 2004). In cases where only the carbonate component of the tooth enamel was reported, a non-species specific $\delta^{18}O_c - \delta^{18}O_w$ equation was used (Ring et al., 2020).

iii. Data Filtering

To perform statistical tests on the data and construct longitudinal gradients through time, both the modern and paleoclimate data were filtered to select samples that received most of their moisture from a westerly source, based on results from HYSPLIT modeling of modern air-mass trajectories and the WAM. For $\delta^{18}O_w$, west of 50°E (Europe), only samples between 47°N-55°N were included in the analysis (Fig. 1). East of 50°E (Asia), only $\delta^{18}O_w$ data between 35°N-55°N were included; 55°N is the northernmost extent of paleo-data in Asia, and thus modern data was also limited to this latitude. $\delta^{18}O_w$ data from southern Europe and Asia (south of 47°N and 35°N, respectively) are excluded from the study due to the influence of other moisture sources (Fig. 1). Data from high latitudes were also removed. The proxy $\delta^{13}C$ in Asia were also filtered to remove samples heavily affected by the South Asian Monsoon, and thus only samples >35°N were considered in construction of $\delta^{13}C$ longitudinal gradients and statistical tests (Rugenstein and Chamberlain, 2018; Ao et al., 2021).

After filtering the data, average $\delta^{18}O_w$ and $\delta^{13}C$ values for both Europe and Asia for each epoch were calculated, and a student's t-test was performed on the mean values to determine statistical significance between Europe and Asia for a given epoch. The longitudinal $\delta^{18}O_w$ and $\delta^{13}C$ gradients were calculated upon filtered datasets using a linear best-fit. Although we do not think that the actual isotopic longitudinal profile decreases linearly across the continent due to a range of thermodynamic and environmental factors (*e.g.*, Rayleigh distillation, influence of moisture recycling), we use a linear approximation as it requires the fewest assumptions regarding $\delta^{18}O$ distillation across the continent. More complex formulations would require more data to

further constrain the shape of the profile. We utilize two methods to compare gradients between epochs: 1) by determining the confidence interval at which the two slopes do not overlap, and 2) by calculating the significance of the difference between two slopes (Cohen et al., 2003; Soper, 2022).

iv. Modeling of $\delta^{18}O$ Gradients

A reactive transport model (hereafter RTM) developed by Kukla et al. (2019) was utilized to construct theoretical longitudinal $\delta^{18}O$ gradients over Eurasia along a transect at 50°N from 10°W to 120°E under varying atmospheric pCO_2. The model uses a reactive transport framework and maintains water mass balance via a Budyko framework for the partitioning of P into ET and q to predict $\delta^{18}O_p$ along a storm track. The RTM is useful in establishing $\delta^{18}O$ gradients based on thermodynamics alone, essentially providing a "null hypothesis" of expected gradients under varying CO_2 regimes to compare against proxy-generated paleo-$\delta^{18}O$ gradients. The RTM generates $\delta^{18}O$ estimates at each grid cell along a single moisture track with no mixing of moisture sources, has no vertical gradients in $\delta^{18}O$, and maintains only linear upslope lifting and condensation over simulated mountain ranges. For further details regarding the reactive transport model, we refer the reader to Kukla et al. (2019).

Reanalysis and model output (Global Land Evaporation Amsterdam Model (GLEAM), Global Precipitation Climatology Center (GPCC), and National Centers for Environmental Prediction-Department of Energy Atmospheric Model Intercomparison Project II Reanalysis (NCEP-DOE AMIP-II Reanalysis (R-2))) were used to populate the parameters in the RTM to construct the modeled modern longitudinal $\delta^{18}O$ gradient (Table 1). The annual mean of each parameter was used. Parameters from Community Earth System Model – Coupled Model Intercomparison Project Phase 6 (CESM-CMIP6) output forced under Pre-Industrial (PI; 280

ppm), two times Pre-Industrial (2xCO_2; 560 ppm), and four times Pre-Industrial (4xCO_2; 1120 ppm) CO_2 concentrations were used to construct theoretical longitudinal gradients under varying atmospheric CO_2 concentrations (Eyring et al., 2016; Danabasoglu, 2019a; 2019b; 2020). These concentrations were chosen as they are analogous to periods of past high-CO_2 in the Cenozoic and thus could be compared to the proxy-generated paleo-longitudinal gradients (Table 2). Inputs into the RTM directly from the CESM output include air temperature, wind speeds and relative humidity (Table 1). Potential evapotranspiration (PET) was calculated following the methods of Ibarra et al. (2018, eqn. 4; Table 1), using CESM output fields of sensible and latent heat fluxes (SH and LE, respectively) and latent heat of vaporization (Lv; 2.501x10^6 J/kg) (PET = (LE+SH) / Lv). Precipitable water (PW) was calculated as the vertical, mass-weighted integral of specific humidity in pressure coordinates from the surface to the top of the atmosphere. Both the PET and PW calculations were performed at each grid cell and each timestep prior to calculating the annual mean. The RTM also requires an estimate of the transpiration fraction of ET, which we estimate as 64% (the global mean estimate from Good et al., 2015). To calculate the degree of water recycled to the atmosphere via ET using the Budyko framework, we must also estimate omega – a variable with no direct physical definition that serves as a watershed-scale parameter and determines the efficiency of moisture recycling and integrates the effects of vegetation, topography, seasonality, and other properties on ET (Budyko, 1974; Kukla et al., 2019). We use 2.6, which is an estimate of the global mean value (Greve et al., 2015).

Additionally, we directly simulate isotopes in the hydrologic cycle using the isotope-enabled version of CESM (iCESM; Brady et al., 2019) forced under Pre-Industrial (iPI; 280 ppm), two times Pre-Industrial (i2xCO_2; 569.8 ppm) and four times Pre-Industrial (i4xCO_2; 1138.8 ppm) CO_2 concentrations. iCESM was run at a roughly 2° resolution (1.9° latitude by 2.5° longitude)

using the Cheyenne supercomputer operated by the National Center for Atmospheric Research Computational and Information Systems Laboratory (CISL; CISL, 2019). The computing hours necessary to run the simulations were acquired through an unsponsored university small request available to graduate students from the CISL. The iCESM simulations simulate the fractionation of ^{16}O and ^{18}O in the atmospheric and land surface parts of the hydrologic cycle, including fractionation from evaporation on the land surface and condensation into clouds and precipitation. The simulations were configured to use only the atmospheric and land-surface models, with prescribed sea surface temperatures and sea ice concentrations (SSTICE) that varied seasonally. The iPI simulation used SSTICE forcing was included with iCESM. The SSTICE forcing for i2xCO_2 and i4xCO_2 were derived from 50 years of model output SST and sea ice data from two CESM2 simulations ("abrupt-2x CO_2" and "abrupt-4x CO_2") included in CMIP6 (Eyring et al., 2016). Each of the three iCESM simulations were initialized with the same $\delta^{18}O$ conditions and were run for 10 years, with only the last 5 years of data used in analysis to account for model spin-up. The $\delta^{18}O$ of precipitation was calculated by computing the isotope ratio of ^{16}O and ^{18}O precipitation rates, which are standard iCESM output fields.

Results

i. Modern $\delta^{18}O_{mw}$

Generally, western Europe exhibits high modern $\delta^{18}O$ values that decrease systematically across the continent (Fig. 2A, B). The lowest values are seen in the Himalayan region, which receives moisture that is isotopically depleted due to orographic forcing of south Asian monsoon rainfall (Wang et al., 2017). The high latitudes also display more negative $\delta^{18}O$ compositions because the high latitudes are colder, leading to a decline in the total precipitable water in the atmosphere and thus larger effective rainout of airmasses as moisture is transported poleward. Regional-scale variations in $\delta^{18}O_{mw}$ result largely from the effects of orographic rainout (e.g., the Alps) and from mixing of moisture sources (e.g., the Mediterranean). Places surrounding the Mediterranean, particularly to the east, have higher $\delta^{18}O_{mw}$ compositions because the $\delta^{18}O$ of moisture derived from this source is higher than that of the Atlantic due to evaporative effects. Central India also has high $\delta^{18}O$ values due to low amounts of distillation coupled with exceptionally large moisture fluxes as moisture is transported from the Indian Ocean inland. Observations among each water type (precipitation, groundwater, river and stream, and tap water) appear to exhibit similar spatial patterns of $\delta^{18}O$ among each other.

ii. Paleo-$\delta^{18}O_{mw}$

The spatial distribution of paleo-$\delta^{18}O_{mw}$ reconstructed from proxy $\delta^{18}O_{c/e}$ largely follows spatial patterns similar to those observed in the modern, but with variations in the absolute value of $\delta^{18}O$ among different geologic epochs (Fig. 3A-F; Table 3). In nearly all epochs, $\delta^{18}O$ values decrease towards the east, as observed in the modern. Similar trends in regional isotopic variation, such as low $\delta^{18}O$ in the high-latitudes and high $\delta^{18}O$ near the Mediterranean, are observed in the

Quaternary. These higher Mediterranean values persist throughout the Miocene. There are no high-latitude samples from the post-Quaternary proxy data to compare to those in the modern and Quaternary. Average proxy-derived $\delta^{18}O_{mw}$ values for eastern Eurasia (>50°E, 35-55°N) remain relatively invariant throughout the Cenozoic, with mean values of filtered data ranging only by ~2‰, between -9.31 ± 1.91‰ (Oligocene; n = 30) and -7.49 ± 1.77‰ (late Miocene; n = 26). Conversely, the average proxy $\delta^{18}O$ composition in western Eurasia (<50°E, 47-55°N) has a much larger range, from -9.30 ± 0.98‰ (Pliocene; n = 8) to -2.47 ± 3.44‰ (late Miocene; n = 9). The lowest mean European $\delta^{18}O_{mw}$ values occur in the modern, Quaternary, and the Pliocene, with earlier epochs of the Cenozoic exhibiting much higher mean isotopic compositions.

The decrease of $\delta^{18}O_{mw}$ with longitude – also termed the "longitudinal gradient" – varies through time. The longitudinal $\delta^{18}O$ gradient is shallowest in the Quaternary and Pliocene, with no statistical significance between the European and Asian $\delta^{18}O_{mw}$ populations in these epochs or between the slopes of these gradients (Fig. 4; Tables 3, 4). The longitudinal gradient steepens further into the Cenozoic, with the steepest gradients in the late Miocene (5-14 Ma), early Miocene (14-23 Ma), Oligocene, and Eocene. These four periods also have statistically distinct $\delta^{18}O_{mw}$ compositions between Europe and Asia, but the changes in the slope of the gradients are not statistically significant (Tables 3, 4). The only period with a statistically distinct change in the slope of the $\delta^{18}O_{mw}$ gradient is between the Pliocene and Late Miocene (Table 4). The modern $\delta^{18}O_{mw}$ longitudinal gradient is dissimilar from that of each other epoch in the Cenozoic.

iii. Paleo-$\delta^{13}C$

Paleosol $\delta^{13}C$ in Asia is consistently elevated compared to that in Europe throughout the Cenozoic (Fig. 5; Table 5). However, the two isotope populations are only statistically distinct during the latter half of the Cenozoic, from the Late Miocene to the Quaternary (Table 5). The

mean $\delta^{13}C$ values in Europe range from -8.66 ± 2.40‰ (late Miocene; n = 8) to -4.49 ± 2.43‰ (early Miocene; n = 1), with the lowest mean value occurring in the late Miocene, and the highest mean value in the preceding geologic sub-epoch of the early Miocene. The carbon isotopic values in Asia range from -5.18‰ (early Miocene; n = 11) to -2.72 ± 2.47‰ (Quaternary; n = 15). Western Asia consistently has higher $\delta^{13}C$ values than in Eastern Asia, whereas no clear pattern in $\delta^{13}C$ can be discerned in Europe. In the Miocene in particular, elevated $\delta^{13}C$ in central Asia are surrounded by lower $\delta^{13}C$ values, as previously shown by Caves et al. (2016). The longitudinal gradient of $\delta^{13}C$ across Eurasia has a positive slope in each epoch except the early Miocene, which is slightly negative (Fig. 6; Table 5). Additionally, differences in longitudinal $\delta^{13}C$ gradients through the Cenozoic are only significant between the early Miocene to late Miocene (Table 6). However, we note that calculations of the Eurasian longitudinal paleosol carbonate $\delta^{13}C$ gradient in the early Miocene through the Eocene are limited by low data density in Europe, with only one datapoint in Europe generating the western portion of the profile in the early Miocene and the Oligocene. Additionally, the confidence intervals do not allow for determination of a positive or negative gradient across the continent for the early Miocene through Eocene.

iv. Reactive Transport Model and iCESM $\delta^{18}O_p$ Gradients

Longitudinal $\delta^{18}O_p$ gradients produced by the reactive transport model and iCESM under varying CO_2 concentrations demonstrate differences in the gradient with differing CO_2 levels. For both the iCESM and RTM results, the steepest gradient is generated with the lowest CO_2 (Pre-Industrial pCO_2) and the shallowest gradient is associated with the highest CO_2 at $4xCO_2$, with the modern and $2xCO_2$ gradients falling between these end-member concentrations (Fig. 7A). The modern gradient generated by reanalysis output mostly lies between the Pre-Industrial and $2xCO_2$ gradients, with variations in the shape of the longitudinal profiles occasionally resulting in the

modern profile falling slightly above the 2xCO_2 gradient. Plotting the modern modeled $\delta^{18}O_p$ profile over observed modern $\delta^{18}O_p$ between 47°-50°N indicates that the gradient and profile generated by the RTM corresponds with that which would be expected from observational compiled data (Fig. 7B).

The shapes of the profiles produced by the RTM are generally similar among the different CO_2 conditions, particularly among the three profiles produced by CESM output (PI, 2xCO_2, 4xCO_2). Each of the CESM profiles are relatively shallow from -10°E to ~0°E; then, the PI and 2xCO_2 profiles steepen dramatically until ~30°E. After this point, those two profiles appear to shallow again, and $\delta^{18}O_p$ tends to not decrease much further until the end of the storm track at 120°E. The CESM 4xCO_2 profile exhibits a roughly linear decrease in $\delta^{18}O_p$ along the entirety of the storm track (excluding the slight increases ~87°E and 92°E). The modern profile presents a slightly different spatial pattern than the CESM- and iCESM-produced profiles, with a steady decrease in $\delta^{18}O$ until ~50°E, after which the profile significantly shallows. Each of the four RTM profiles exhibit increases in $\delta^{18}O_p$ around 87°E and 92°E, at the location of the Altai Mountains in Mongolia. These increases likely do not occur in actual $\delta^{18}O_p$; because we did not simulate topography while running the RTM, changes in hydroclimate parameters that are induced by orography (high P, low T, etc.) in the reanalysis and CESM input are not resolved correctly and thus show slight increases, where in reality the profile would decrease due to rainout at this mountain range.

The iCESM gradients, although generally in agreement with the "high-CO_2 generates shallow gradients" result from the RTM run with CESM output, exhibit slightly different results than the RTM gradients. The shape and slope and the i2xCO_2 and i4xCO_2 profiles are fairly like that of the 4xCO_2 CESM-RTM profile but have a lower initial $\delta^{18}O_p$ that results in an overall

downward shift in the modeled $\delta^{18}O_p$ along the storm-track. The i2xCO_2 profile varies little from the i4xCO_2 profile, whereas the 2xCO_2 profile tends to fall in the center of the PI and 4xCO_2 profiles. The iPI profile varies quite dramatically from that of the Pre-Industrial CESM-RTM profile; the iPI profile stays fairly shallow until ~70°E, at which point a marked decrease in $\delta^{18}O_p$ is produced where the transect reaches the Altai Mountains. The iCESM profiles produce the expected decrease in $\delta^{18}O_p$ at the Altai Mountains because iCESM accounts for topography, unlike the RTM.

Discussion

The compilation of stable O and C isotopes across Eurasia allows us to explore the evolution of hydroclimate and paleoclimate in this region throughout the Cenozoic. Herein, we discuss the general response of the model and proxy $\delta^{18}O$ gradients to changes in pCO_2. We then consider the different responses of the proxy and modeled $\delta^{18}O$ gradient to varying pCO_2, which may be explained by 1) proxy-related mechanisms, including poor preservation of proxy materials resulting in changes in $\delta^{18}O_{c/e}$ through time or changes in seasonality of proxy formation through time; 2) shifts in climate and paleogeography that alter $\delta^{18}O_p$; and/or 3) changes in paleoclimate parameters that are not accounted for in either the RTM or ESMs. We also consider the implications of the spatial distribution and changes in $\delta^{13}C$ for primary productivity and discuss why the temporal shifts in $\delta^{13}C$ likely do not predominantly record changes in global atmospheric pCO_2 or spread of C4 vegetation.

i. Proxy-model comparison of longitudinal $\delta^{18}O$ gradients

Changes in precipitable water (PW) with increased atmospheric CO_2 appear to drive the observed variations in the modeled slope of longitudinal $\delta^{18}O$ gradients across Eurasia. As previously discussed, the Clausius-Clapeyron relation states that atmospheric water content increases by 7% per each degree of warming (Held and Soden, 2006). However, although global mean precipitation is sensitive to this relation, it does not scale at this rate; rather, this parameter scales with the Earth's energy budget and has a much lower sensitivity of ~2%/K (Held and Soden, 2006; Stephens and Hu, 2010; Pendergrass and Hartmann, 2014). Because of the differential rates of increase between PW and P with warmer temperatures, with PW increasing faster than P, the reservoir of ^{18}O in the atmosphere is less affected by removal by P, reducing any changes in $\delta^{18}O$

(van Dijk et al., 2020; Figure A3). This "buffering" reduces the fraction of moisture removed by rainout across the continent, thus shallowing the $\delta^{18}O$ longitudinal gradient at high pCO_2. The results of the RTM indicate that, based on thermodynamics alone, one would expect longitudinal $\delta^{18}O$ gradients to shallow in a higher CO_2 world.

The results from the proxy-generated paleo-$\delta^{18}O_w$ longitudinal gradients, however, indicate the opposite response – proxy data suggests that steeper longitudinal gradients are associated with higher pCO_2. During periods of known high atmospheric pCO_2, such as the Eocene, Oligocene, and Miocene, the longitudinal gradients observed are significantly steeper than during periods of low pCO_2, like the Pliocene, Quaternary, and in the modern (Beerling and Royer, 2011; Anagnostou et al., 2016; Mejía et al., 2017). Because the mean $\delta^{18}O_w$ of proxy data in Asia has remained similar through the Cenozoic, varying only by ~2‰ from the Eocene to the Quaternary, the shallowing of the gradient during the Cenozoic is caused primarily by a decrease in the mean $\delta^{18}O_w$ in Europe, which has decreased by ~7‰ between the Eocene and now. The largest shift in $\delta^{18}O_w$ in Europe occurs between the late Miocene and the Pliocene – prior to this point, $\delta^{18}O_w$ in Europe was relatively invariant, ranging only from -2.47‰ to -3.25‰ (Table 3). However, a major decrease then occurs, shifting the average $\delta^{18}O_w$ in Europe from -2.47‰ in the late Miocene to -9.30‰ in the Pliocene. This negative shift in the $\delta^{18}O_w$ over Europe in the Pliocene drives the shallowing of the slope observed in this same epoch, as the values in Europe shifted closer to those observed in Asia.

a. Proxy-related mechanisms – is the $\delta^{18}O$ signal real?

The $\delta^{18}O$ preserved in authigenic materials may be altered from the original meteoric water signal through diagenesis and/or evaporative enrichment. Diagenesis may occur when carbonate is exposed to increased temperatures – for example, through burial – inducing a temperature-

dependent fractionation that lowers the $\delta^{18}O$ preserved in the mineral lattice (Garzione et al., 2004). Carbonate diagenesis may also occur in the presence of meteoric water with a different isotopic composition than the original composition of the water in which the mineral formed, which can result in either raising or lowering the $\delta^{18}O_c$ to reflect the $\delta^{18}O$ of the more recent fluid. Generally, older minerals are more likely to have experienced diagenesis simply due to their longer exposure to either higher temperatures or waters with different $\delta^{18}O$ compositions. However, the compiled studies have been filtered for known indications of diagenesis in each proxy type (*i.e.,* petrographic analysis, covariance of O and C, and variation in the expected offset of 8‰ of enamel phosphate and carbonate $\delta^{18}O$). Further, diagenesis tends to lower $\delta^{18}O_c$, whereas higher $\delta^{18}O$ is observed in the distant past in Europe. Thus, diagenetic effects can be eliminated as driving the divergent response of the proxy and model $\delta^{18}O$ gradients to CO_2.

Evaporation imparts the opposite signal on $\delta^{18}O_c$; when lake water evaporates, ^{16}O preferentially evaporates into the vapor phase, leaving the water in which carbonate forms enriched in ^{18}O and thus increasing the $\delta^{18}O_c$ above $\delta^{18}O_{mw}$. Covarying $\delta^{18}O$ and $\delta^{13}C$ is a primary indication of evaporative enrichment of lacustrine samples (Horton et al., 2016; San Jose et al., 2020). The Asia stable isotope data have been previously screened for evaporative effects and none were found, given that the lacustrine and paleosol data overlap (Rugenstein and Chamberlain, 2018). The Europe stable isotope data was screened for evaporative effects by plotting $\delta^{18}O$ vs. $\delta^{13}C$ to investigate covariation in lacustrine samples; only the mean of the lowest 20% of samples from those locations are included in our analyses and figures (Rowley and Currie, 2006; Cyr et al., 2005; Li et al., 2015). However, even if lacustrine samples are removed from statistical analyses, similar trends are observed in the data (Fig. 4A-F, red dashed line; Tables A1-2). The same general trend of shallowing of the gradient throughout the Cenozoic with and without lacustrine proxy data is

still observed. Additionally, although the gradient with no lacustrine data shallows in the Eocene, Oligocene, and Miocene relative to the with-lacustrine gradient (Fig. 4A-F, red dashed line), we observe that both with and without lacustrine samples, the only period with a statistically significant change in the slope of the gradients is between the late Miocene and Pliocene, implying the results are robust even after removing those samples most likely affected by evaporation. Finally, in each epoch (except the Miocene), there are other non-lacustrine proxy data with similarly high $\delta^{18}O$ values, suggesting the high $\delta^{18}O$ in the early Cenozoic is not merely an evaporative effect.

Differences in the type of meteoric water (*i.e.,* precipitation, soil water, or river water) incorporated in authigenic carbonates and changes in the seasonality of proxy formation may result in shifting $\delta^{18}O_c$ values through time but are unlikely to completely explain the divergent data-model $\delta^{18}O$ gradients. As previously discussed, paleosol carbonates form in the soil column, and thus incorporate soil water $\delta^{18}O$ during mineralization. This water is primarily sourced from precipitation, resulting in a mixture of $\delta^{18}O$ from individual precipitation events and seasons in the soil (Breecker et al., 2009; Lachniet, 2009). Paleosol carbonates are thought to form during warm and dry periods, with carbonate precipitation driven by increasing temperature, increasing calcium ion activity due to increased ET, and decreasing soil CO_2 (Breecker et al., 2009; Huth et al., 2019). Lacustrine carbonates predominantly record the $\delta^{18}O$ of local precipitation. The size of the lake, and related water residence time, affects both the amount of seasonal variation and the amount of evaporation that may alter the $\delta^{18}O$ of the lake and thus $\delta^{18}O_c$ (Leng and Marshall, 2004). Speleothem carbonates precipitate from water that infiltrates downward from the surface to the ceiling of an underlying cave and thus the $\delta^{18}O_c$ is a function of precipitation and recharge seasonality, as well as modification within the soil and epikarst (White, 2019; Lachniet, 2009).

These carbonates are thought to accumulate calcite mostly during cooler seasons, with little to no accumulation in the warm season (James et al., 2015). Mammal tooth enamel $\delta^{18}O$ is largely sourced from the animal's body water, which in turn reflects local meteoric water taken in through drinking and eating (Kohn, 1996; Kohn and Cerling, 2019; Kohn and Law, 2006). Mammal tooth enamel has the potential to record seasonal variations in $\delta^{18}O$, but sampling techniques often average these effects, and thus often report a time-averaged $\delta^{18}O$ signal from the period of enamel formation which can range from weeks to years (Kohn, 2004; Blumenthal et al., 2014). Therefore, each of these proxies generally reflect local precipitation, although secondary influences such as evaporation, seasonality, and time-averaging of $\delta^{18}O$ might influence the absolute $\delta^{18}O$ recorded by the proxy. However, because we have screened for evaporative effects (which are most likely to impact lacustrine carbonates), because we take a multi-proxy approach which should ameliorate many proxy-specific biases, and because different proxies that formed in relatively close locations record similar $\delta^{18}O_w$ (Fig. 3A-F; Caves et al., 2016), we conclude that differences in the $\delta^{18}O_{mw}$ incorporated by each of the proxies are effectively reduced and thus do not significantly impact the interpretation of past $\delta^{18}O$ longitudinal gradients.

Changes in the seasonal timing of proxy formation could drive variation in the $\delta^{18}O$ preserved during mineralization. Although conditions that tend to produce paleosol carbonates (warm, dry periods) fall during the summer months across much of modern Eurasia, particularly in eastern Eurasia (Beck et al., 2018; Nagavciuc et al., 2022), changes in past climate may have shifted carbonate formation to different times of year (Methner et al., 2020; Kukla et al., 2022b). Changing seasonality of proxy formation would impart a significant effect on the $\delta^{18}O_w$ recorded by these materials because $\delta^{18}O_p$ is highly seasonally variable. During cold months, $\delta^{18}O_p$ is substantially lower than during the warm months due to the lessened capacity of cold air parcels

to retain moisture as compared to warm air; precipitation $\delta^{18}O$ thus peaks during the hot summer months and is lowest during the cold winter months (Rozanski et al., 1993). Shifts in precipitation seasonality in Eurasia (*i.e.,* shifting carbonate formation to the spring or fall due to increases in summer precipitation), could thus result in decreased $\delta^{18}O_c$. Moreover, changes in seasonality in Europe but not in Asia could explain the relative stability of mean $\delta^{18}O_w$ in Asia co-occurring with large decreases in mean European $\delta^{18}O_w$ between the late Miocene to Pliocene, Quaternary, and modern. Recent modeling of precipitation seasonality by Brönnimann et al. (2018) in the Alpine region predicts shifts in heavy precipitation events from the late summer to early summer and autumn under warmer conditions (RCP 8.5) over the next century. If past conditions during warm periods in Europe (Eocene, Oligocene, and Miocene) exhibited this same pattern of seasonality, carbonate formation would have been favored during hot, dry summer conditions, and therefore carbonate $\delta^{18}O_c$ would record the highest possible $\delta^{18}O_p$. Overall cooler conditions during the Pliocene, Quaternary, and in the modern may have driven precipitation seasonality toward peak rainfall in the summer months, thereby shifting the timing of carbonate formation to a cooler, drier season and thus producing a negative shift in $\delta^{18}O_c$. Therefore, shifting seasonality of carbonate formation in Europe may drive the shallowing of the gradient in the late Cenozoic.

b. Paleogeographic and paleoclimatic changes

Another potential explanation for the contradiction between the modeled and proxy response to CO_2 is the effect of shifting paleogeography and paleoclimate on proxy $\delta^{18}O$; such changes are not accounted for in the modeled $\delta^{18}O$ gradients. Two of the largest differences between modern geography and paleogeography are moisture sources and orography. During the Mesozoic and early Cenozoic, the Tethys Ocean allowed water transport between the Atlantic, Indian, and Pacific oceans, imparting a large effect on global climate and ocean circulation (Rögl,

1999). This ocean shrank with northward plate motion of the African, Australian, and Indian plates from the late Cretaceous through the Oligocene, eventually leading to creation of the enclosed Mediterranean, Caspian, and Black Seas (Rögl, 1999; Bialik et al., 2020). This plate motion, combined with global sea level decline, also culminated in the formation of the Paratethys in the early Oligocene (Popov et al., 2006). The Paratethys was a separate inland sea that covered much of central Europe and west Asia (Fig. A4) and was disconnected from the Tethys to the south by mountains produced during the Alpine orogeny (Rögl, 1999). Termination of the seaway connecting the Indian and Atlantic oceans occurred around the middle Miocene (~16-14 Ma) and coincided with a period of cooling – likely driven by lower pCO_2 – known as the Mid-Miocene Climate Transition (MMCT) (Rögl, 1999; Hamon et al., 2013; Simon et al., 2019). This coeval closure and cooling resulted in a substantial enhancement of the Atlantic Meridional Overturning Circulation (AMOC) by transporting warm and saline water from the proto-Mediterranean to the Atlantic Ocean (Hamon et al., 2013; Verducci et al., 2009), and an enhancement of North Atlantic Deep Water (NADW) production and meridional heat transport, resulting in modern-like ocean circulation dominated by the NADW (Hamon et al., 2013). Another consequence of cooling at the MMCT was Southern Hemisphere glaciation that led to eustatic sea level fall and disconnection between two Paratethyan basins (Fig. A4; Shevenell et al., 2008; Simon et al., 2018; Holbourn et al., 2007). Detachment and lower water level in these two basins resulted in overall less evaporation of moisture because of a reduction of water surface area, largely caused by aerial exposure of shallow marginal regions (Simon et al., 2018).

Northern Hemisphere glaciation may have contributed to the significant shallowing in the gradient between the steep gradients of the Eocene, Oligocene, and Miocene and the shallow gradients in the Pliocene, Quaternary, and modern. Northern Hemisphere glaciation initiated

around 3.6 Ma in the late Pliocene and later intensified around the Pliocene-Quaternary boundary (~2.7-2.8 Ma) due to either declining atmospheric pCO_2 or the closure of the Central American Seaway (Mudelsee and Raymo, 2005; Ruggieri et al., 2009; Lunt et al., 2008; Haug and Tiedemann, 1998). Both proxy and modeling-based studies indicate that glaciation was amplified by intensification of AMOC (Hayashi et al., 2020; Lunt et al., 2008). Glaciation had major effects on atmospheric circulation; the NH midlatitude westerlies were likely weaker and more poleward during the warmer early Pliocene, then stronger and shifted equatorward after the intensification of glaciation ~2.7 Ma (Abell et al., 2021; Dolan et al., 2015; Xiangyu et al., 2015). Stronger westerly winds may have induced the more recent shallower gradients in $\delta^{18}O$ by reducing the ability of air parcels to rainout over a continent, allowing for proportionately lower overall rainout.

However, if strong westerlies were the sole cause of the gradient shallowing, then one would likely expect to see European $\delta^{18}O$ values remain relatively invariant, while $\delta^{18}O$ values would increase in Asia, as there would be progressively less rainout with stronger winds across the continent. Instead, the opposite is observed – the gradient shallows because of a downward shift in mean $\delta^{18}O$ in Europe in the Pliocene and Quaternary, whereas mean $\delta^{18}O$ in Asia remains relatively low. Weaker westerlies may still explain a relative shallowing of the gradient but cannot explain why the initial $\delta^{18}O$ over the western part of the Eurasia decreases between the late Miocene and the Pliocene. The lowering of Europe $\delta^{18}O$ may be partly due to the location of samples from the Pliocene, which are located in modern-day Hungary and Slovakia. By the time an air parcel sourced from Atlantic moisture has reached that far inland, a decrease of at least 2-3‰ has likely already occurred, and thus this inland $\delta^{18}O$ value doesn't represent the 'initial' $\delta^{18}O$ rained out from the air parcel over land (McDermott et al., 2011; Rozanski et al., 1993). Additionally, because the only samples from the Pliocene that fall within the filtered range of

'westerly' moisture are of the same proxy type (mammal tooth enamel) and constrained to a small location, it is difficult to base the entirety of the European portion of the gradient on these few samples. We can thus more confidently say that the gradient shallows by the Quaternary, and possibly as early as the Pliocene. More data is needed from western Europe in the Pliocene to constrain the timing of the gradient shallowing and thus explicate the relationship between reduced atmospheric pCO_2, global cooling, weakening of the westerlies, shifts in seasonality of proxy formation, and the negative shift of Europe $\delta^{18}O$.

Although changes in moisture sources and atmospheric circulation resulting from growth and decline of the Tethys, Paratethys, and Northern Hemisphere glaciation appear to potentially contribute to shallowing the gradient in the Pliocene, Quaternary, and modern, these factors likely cannot explain the varying response of proxy and model gradients under different atmospheric CO_2 concentrations. To reiterate, the proxy data produce steeper gradients during epochs of higher CO_2 (Eocene-Miocene), whereas the modeled gradients illustrate the opposite response. If changes in the gradient were driven purely by moisture source changes throughout the Cenozoic, one would likely observe a shallower gradient coinciding with the existence of the Tethys and Paratethys in the early Cenozoic because these additional moisture sources would replenish depleted airmasses with higher $\delta^{18}O$ relative to the existing $\delta^{18}O$ in the atmosphere. Oceans have $\delta^{18}O$ values near 0‰; thus, moisture supplied to the atmosphere by the Paratethys or Tethys would shallow the gradient over the continent by contributing higher $\delta^{18}O$ than that of the existing airmass. After the closure of those moisture sources by the late Miocene, incoming moisture to Asia would have travelled over the continent without replenishment from this high $\delta^{18}O$ source and must have lower $\delta^{18}O$ as a result, which would steepen the gradient. The opposite response is observed – the steepest longitudinal gradients coinciding with peak spatial extent of these large moisture sources suggests

that changes in moisture sources are not primarily driving the steep gradients associated with periods of high atmospheric CO_2. Therefore, while changes in paleogeography that result in shifting moisture sources may explain the changes observed among epochs in the proxy gradients (*i.e.,* shallowing from the late Miocene to Pliocene-Quaternary), they cannot account for the opposing responses to higher atmospheric pCO_2 between the modeled and proxy gradients.

Uplift of ranges across Eurasia during the Cenozoic also fails to explain the contradiction between the proxy and modeled gradients due to a likely minimal effect from topographic changes on longitudinal $\delta^{18}O$ gradients. Across Eurasia, the Cenozoic was a time of significant topographic changes due to northward movement of the Indian, African, and Australian plates. In Asia, initial collision of the Indian and Eurasian plates is estimated to have occurred ~55 Ma (DeCelles et al., 2014), and by the mid-Miocene, most of Tibet had achieved high elevations and the plateau had begun to form (Rowley and Garzione, 2007; Wang et al., 2014a; Rohrmann et al., 2012; Li et al., 2015). Meanwhile, in Europe, the alpine orogeny that eventually led to the creation of many E-W oriented ranges (including the Pyrenees, Alps, Apennines, Dinaric Alps, Carpathians, Caucasus, etc.) had initiated by the Eocene-Oligocene Transition (Meulenkamp and Sissingh, 2003; Handy et al., 2010), with near-modern elevation for the Alps reached around the mid-Miocene (Campani et al., 2012; Krsnik et al., 2021). Orography drives high rates of rainout from air masses (thus lowering $\delta^{18}O_p$), which results in substantial reduction of water vapor transport into continental interiors on the leeward side of ranges. Theoretically, uplift may therefore result in a steepening of longitudinal $\delta^{18}O$ gradients, and hence one would expect to see gradients begin to steepen at the onset of uplift, with significantly steeper gradients during times of maximum elevation of these ranges.

However, there is little evidence that changes in paleoelevation drive changes the gradient produced by westerly moisture across Eurasia due to the orientations and locations of uplifted ranges. Primarily, because the ranges in Europe are oriented in an E-W direction, they present a much narrower barrier to moisture transport by the westerlies than if they were oriented N-S, in which case they would act as meridional barriers to the westerlies (Broccoli and Manabe, 1992). Studies that use proxy data to reconstruct timing of the onset of central Eurasian aridity link continental aridity to global cooling (producing a subsequent reduction of vapor pressure and hence inland moisture transport) and uplift of the Tibetan Plateau, suggesting that these airmasses transported by the westerlies are depleted not by orographically-forced rainout over Europe but by rather by global climatic conditions and teleconnections due to remote orography (Broccoli and Manabe, 1992; Tang and Ding, 2013; Liu et al., 2009; Li et al., 2018). Altitudinal effects on $\delta^{18}O$ resulting from high intensity rainout have spatially limited effects on regional $\delta^{18}O$ in Europe, but orographic rainout from these relatively small ranges is unlikely to significantly affect both inland vapor transport and a $\delta^{18}O$ gradient spanning nearly 8,000 km in length, wherein progressive rainout and moisture recycling over the continent dominate the $\delta^{18}O$ signal. Several climate modeling studies focusing on the Miocene reach similar conclusions that the impact of paleogeographic differences on global mean atmospheric temperature are small (although not insignificant), and suggest that vegetation differences are more impactful on global climate (Knorr et al., 2011; Bradshaw et al., 2012; Herold et al., 2011)

Furthermore, European ranges appear to block predominantly Mediterranean moisture from traveling northward into central Europe given their orientation and proximity to this moisture source, rather than blocking Atlantic/westerly driven moisture. This is demonstrated through both the HYSPLIT (Fig. 1) and modern $\delta^{18}O_{mw}$ (Fig. 2A) results, as well as from studies of high-

intensity precipitation events and sources of Alpine moisture. HYSPLIT indicates that northward of 47°N, the Mediterranean is not a major source region of air parcels travelling over Eurasia (Fig. 1). Similarly, studies of modern floods and high-intensity precipitation events in central and eastern Europe indicate that most of the moisture contributing to these events was sourced from North Atlantic moisture and moisture recycled from the land surface, with minimal contribution from the Mediterranean (Kelemen et al., 2016; Winschall et al., 2014; Gangoiti et al., 2020). Sodemann and Zubler (2010) demonstrate that the northern Alps source more moisture from the North Atlantic, and the southern Alps receive most moisture from the Mediterranean. (Fig. 2A). Isotopic evidence supports this – if moisture north of the Alps was significantly sourced from the Mediterranean, the isotopic signal north of the Alps would remain depleted, rather than increase as observed in the compiled modern $\delta^{18}O_{mw}$ data. This provides significant evidence for minimal effect of the Alps and other E-W orientated ranges on the longitudinal $\delta^{18}O$ gradient and suggests that these ranges help to maintain a transect of westerly sourced moisture across Eurasia that is nominally mixed with other moisture sources by acting as moisture transport barriers.

Similarly, the Himalayas effectively suppress moisture transport northward from the Indian Ocean, as evidenced by the extreme rainout observed on the southern margin of the range (Fig. 1; Fig. 2; Wang et al., 2017; Caves et al., 2015). Modeled simulations of Eurasia with and without topography from Broccoli and Manabe (1992) suggest that the arid conditions in central Asia can only be produced with the presence of high topography in the Tibetan Plateau, which generates a rain shadow on the northern side of the range. This is supported by $\delta^{18}O$ evidence from Caves et al., (2015; now also compiled in this study) that shows consistently low $\delta^{18}O$ throughout the Cenozoic directly in the leeside of the Himalayas (Fig. 3A-F), suggesting that southerly-sourced moisture is largely rained out over the Himalayas, which generate a topographic barrier that has

potentially existed for more than 50 million years between westerly and southerly moisture. Thus, the uplift and presence of these ranges both in Europe and Asia likely had minimal impact on westerly moisture transport and $\delta^{18}O$ gradients across Eurasia throughout the Cenozoic, and at most acted as barriers to mixing between westerly and southerly (Mediterranean Sea, Indian Ocean, etc.) moisture.

c. Model parameterizations

Discrepancies between the parameterization of climate variables in either the CESM, iCESM, or RTM versus actual past hydroclimate conditions may drive the contradiction in proxy-model results. Specifically, the partitioning of precipitation that falls over land into runoff (q) and ET is difficult to constrain under warming and has potential to dramatically shift the isotopic gradient. Empirical studies demonstrate that under higher CO_2 conditions, plant stomata open less which reduces the amount of transpiration per mole of CO_2 consumed (Eamus and Jarvis, 1989; Woodward, 1993). Field experiments indicate the same response, with varying degrees of decrease in stomatal conductance depending on plant type (Li et al., 2003; Kimball et al., 1993; Ainsworth and Rogers, 2007). However, other climatic and plant physiological responses complicate this. Some suggest that due to CO_2 fertilization, plants may produce more leaves or leaf area may increase, resulting in an overall transpiration increase (Piao et al., 2007; Eamus and Jarvis, 1989); similarly, increases in temperature may drive higher vapor pressure deficits which may increase transpiration (Eamus and Jarvis, 1989; Manea and Leishman, 2015). However, models and field observations tend to show that neither increases in leaf area nor temperature are sufficient to outweigh the influence of decreasing stomatal conductance under higher CO_2, and thus many conclude that higher CO_2 results in decreased transpiration (Swann et al., 2016; Lemordant et al., 2018; Kirschbaum and McMillan, 2018; Milly and Dunne, 2016; Skinner et al., 2018).

Increased evaporative demand from higher temperatures and saturation vapor pressure suggests that one can expect an overall PET increase under higher CO_2 conditions (Scheff et al., 2017; Scheff et al., 2014; Milly and Dunne, 2016; Ibarra et al., 2018), but the effect on actual ET is less clear, likely regionally specific, and of smaller magnitude than predicted by Clausius-Clapeyron (Leipprand and Gerten, 2006; Vahmani et al., 2022; Katul et al., 2012). Regardless of absolute changes in ET, high-CO_2 induced warming is likely to simultaneously decrease transpiration and increase evaporation – due to plant physiology and temperature, respectively – leading to a lower transpiration fraction of ET (T/ET ratio) and greater relative importance of E in overall recycling of moisture (Kirschbaum and McMillan, 2018; Vahmanni et al., 2022). Because evaporation and transpiration impart differing fractionations on $\delta^{18}O$, with evaporation preferentially returning ^{16}O to the atmosphere and transpiration having no net fractionation, the T/ET ratio substantially influences the steepness of the longitudinal gradient and may explain the discrepancies in the response of the proxy and modeled $\delta^{18}O$ gradients to higher CO_2. ET with a greater fraction of E results in a replenishment of moisture that is more negative back up to the atmosphere, steepening the gradient. Conversely, a greater fraction of T returns moisture that is relatively less negative, shallowing the continental gradient.

While the T/ET ratio determines the isotopic composition of moisture returning to the atmosphere, a related parameter in the RTM, omega (ω), controls the partitioning of P into q and ET. ω has no physical meaning but serves as a watershed-scale parameter that determines the efficiency of moisture recycling and integrates effects of vegetation, topography, seasonality, and other properties (Kukla et al., 2019). The global average value of ω is ~2.6 (Greve et al., 2015); the theoretical lower limit of ω is 1, which indicates a watershed wherein there is no ET and P is partitioned entirely to runoff, thereby steepening the isotopic gradient across the continent by

reducing (or eliminating) the amount of moisture resupplied to air parcels. Although regional predictions of ω are difficult to constrain, one would predict that global ω should decrease under higher pCO_2 conditions due to a decrease in T (and hence in overall ET). Therefore, the proxy record aligns with theoretical constraints on T, ET, and ω with higher CO_2 – increases in CO_2 likely reduce T, which steepens the gradient by returning proportionately more ^{16}O to the atmosphere through E. Similarly, this lower ET due to decreased T drives lower ω, additionally reinforcing a steeper gradient by reducing the return of terrestrial moisture back to the atmosphere.

Each of the models we utilized to simulate the isotopic gradient across Eurasia have these variables (ET and q) incorporated into their analyses, but changes in these parameters resulting from higher atmospheric pCO_2 may be misrepresented. In the RTM, we set a constant value of the transpiration fraction of ET as 64%, a global estimate of modern ET from Good et al. (2015). The input of a modern T-fraction of ET in the RTM may be an overestimation of the transpiration flux of ET in a warmer world, causing the gradient to shallow with increased CO_2 in the RTM, when in actuality the gradient may steepen due to a decrease in the T/ET ratio with higher CO_2. The estimate of global T-fraction of 64% may itself be incorrect, with estimates from other studies suggesting 57%, 61%, or even a range of 38-77% due to uncertainties in variables such as interception, root dynamics, soil evaporation, and seasonal changes in the T/ET ratio (Wei et al., 2017; Schlesinger and Jasechko, 2014; Wang et al., 2014b). Similarly, the use of the global value of ω (2.6) may be an overestimation for high-CO_2 periods. An overestimation of both plant water use and of the ratio of ET to q would shallow the gradient simulated by the model in comparison to gradients produced by the proxy data during past periods of high pCO_2. Additionally, both T-fraction and ω are set as constant across the 120° transect in the RTM, whereas these variables

likely shift substantially across Eurasia due to changes in the land surface such as topography and vegetation.

The parameterization of E, T, and q in both CESM and iCESM are more intricate than in the RTM, and detailed discussion of the differences between the simple RTM and more complex iCESM results are beyond the scope of this paper. However, it is noted that past studies on CMIP5, CMIP6, and the Community Land Model 4 indicate a range of modeled responses of the T/ET ratio to increased pCO_2. Community Land Model 4 was found to simulate excessive photosynthesis and transpiration in temperate regions (Lawrence et al., 2011). Results from CMIP5 suggest that transpiration (both absolute and as a fraction of ET) is projected to decrease with warming in the tropics and that models underestimate the transpiration fraction of ET in the tropics, while the middle to high latitudes do not trend in any particular pattern; thus, ET changes may vary spatially due to shifts in radiative and physiological drivers that can affect the components of ET in different way in disparate regions (Wei et al., 2017; Berg and Sheffield, 2019). Using CMIP6, Dong et al. (2022) observe a negative T/ET bias across the central United States, while Nooni et al. (2021) find that ET estimates across continental Africa indicate distinct spatial variation in average annual ET across diverse climates. Model comparisons thus seem to indicate a non-uniform response of ET and its components to elevated pCO_2 across different regions.

ii. $\delta^{13}C$ and paleo-productivity

Herein, we interpret changes in the spatial distribution of $\delta^{13}C$ of paleosol carbonates across Cenozoic Eurasia as largely driven by shifts in soil respiration and primary productivity, rather than the traditional use of $\delta^{13}C_c$ as a proxy for past atmospheric CO_2 concentrations or C3 vs. C4 vegetation cover (Cerling, 1999). Changes in vegetation type likely cannot account for observed shifts in proxy $\delta^{13}C_c$ through the Cenozoic; the plant and mammal tooth fossil records indicate that

although C4 plants evolved as early as the middle Eocene, C4-dominated habitats only arose in the middle to late Miocene (Edwards et al., 2010), meaning that for much of the time period covered by our compilation, C4 vegetation was likely not abundant enough to significantly alter the $\delta^{13}C$ of soil carbonates. We additionally rule out C4 influence in the latter part of the Cenozoic, after the rise of C4 grasslands, because there is little evidence for C4 vegetation from other proxies or in the modern distribution of these plants in many of the locations considered in our study (Caves et al., 2016; Still et al., 2003; Rugenstein and Chamberlain, 2018). Fossil tooth enamel records in western Europe show no evidence for C4 dominance over the past 20 Ma, which is consistent with the modern dominance of C3 plants in Europe (Cerling et al., 1997). There is evidence for shifts toward C4 dominance in South and East Asia 8.5 Ma and 6.0 Ma (Cerling et al., 1997; Badgley et al., 2008), but these shifts are focused south of the Himalaya and in East Asia, where we have few data points (Rugenstein and Chamberlain, 2018).

We also conclude that spatial variation in the $\delta^{13}C_c$ record is not primarily driven by changes in atmospheric pCO_2 – barring the influence of different vegetation types, the $\delta^{13}C$ of soil carbonates will record a ratio between atmospheric pCO_2 and soil productivity, with lower pCO_2 driving lower $\delta^{13}C_c$ values, and vice versa (Cerling, 1984; 1991). If the changes in $\delta^{13}C$ were dominantly driven by the decline in global pCO_2 $\delta^{13}C$ through the Cenozoic, rather than by soil respiration rates, we would expect to observe a uniform decrease in $\delta^{13}C_c$ in both Europe and Asia. However, only the $\delta^{13}C_c$ in Europe has decreased over the Cenozoic, while $\delta^{13}C_c$ in Asia has increased over the same interval, suggesting that pCO_2 is not the primary driver of these $\delta^{13}C_c$ changes, particularly in Asia. Thus, the general decline in atmospheric CO_2 concentrations throughout the Cenozoic may contribute to the decrease in Europe $\delta^{13}C_c$, but clearly cannot explain

the increase seen in Asia (Rugenstein and Chamberlain 2018). The subsequent discussion of $\delta^{13}C_c$ will therefore focus on this proxy as an indicator of changes in paleo-productivity.

Instead, we attribute the spatial and temporal distribution of $\delta^{13}C_c$ across Eurasia through the Cenozoic Era can be attributed to variations in primary productivity. On long timescales, soil respiration rates must be positively correlated with productivity (Bond-Lamberty and Thompson 2010); low $\delta^{13}C_c$ reflects higher soil respiration and thus higher productivity. Modern primary productivity is generally high in Europe and low in northern Asia, with the highest gross primary productivity in southeast Asia due to monsoonal moisture (Jung et al., 2011). Caves et al. (2016) and Rugenstein and Chamberlain (2018), who originally compiled the data from Asia in this study, show that the increase in Asia $\delta^{13}C_c$ throughout the Cenozoic must be driven by a decrease in primary productivity and increased aridity to counteract the effect of decreasing atmospheric pCO_2 on $\delta^{13}C_c$. The large increase in $\delta^{13}C_c$ in Asia between the late Miocene and the Pliocene/Quaternary indicates that the region become substantially drier and less productive during this period, and thus the higher $\delta^{13}C_c$ results from some combination of decreased MAP, reduced discrimination in plants against ^{12}C because of water stress, and/or shallowing carbonate formation depth. The decrease in Europe $\delta^{13}C_c$ through the Cenozoic could be either a pure representation of the decrease in atmospheric pCO_2, or a combination of a cooccurring decrease in atmospheric pCO_2 and increased or relatively constant primary productivity. The large decrease in Europe $\delta^{13}C_c$ between the early and late Miocene (-4‰) could be explained by the decrease in atmospheric CO_2 following the MMCT at 14 Ma, with estimated mean pCO_2 falling from ~450 to ~300 ppm (Super et al., 2018; Badger et al., 2013). Regardless, the consistently lower $\delta^{13}C_c$ in Europe suggests that plant productivity has been higher in Europe than in Asia throughout the Cenozoic. Further, the

contrasting trends in $\delta^{13}C$ between Europe and Asia suggest that the difference in plant productivity across the continent has only increased over the course of Cenozoic cooling.

iii. Implications

Combined, the $\delta^{18}O$ and $\delta^{13}C$ records in Eurasia provide insight into the response of the terrestrial hydrologic cycle to shifts in paleogeography and in atmospheric pCO_2. The results from $\delta^{18}O$ recorded in proxy materials suggest that atmospheric circulation across Eurasia has only been marginally impacted by the dramatic changes in paleotopography throughout the Cenozoic, and that major shifts in global climate due to changing pCO_2 instead drive the changes are observed in the proxy record. Similarly, despite substantial changes in moisture sources across Eurasia, the waning of large-scale inland seas across the Cenozoic appears to have surprisingly small effect on moisture transport – it appears that transport was similar to the modern, with the Atlantic providing much of the oceanic moisture over western Europe that is then recycled across the eastern portion of the continent. The sharp decline in European $\delta^{18}O$ during the Pliocene implies that Cenozoic cooling induced large-scale shifts in precipitation seasonality, and the shallowing of the gradient at the Miocene-Pliocene transition perhaps records the strengthening of the westerlies. The persistence of the west-to-east isotopic $\delta^{18}O$ gradient throughout the Cenozoic indicates that moisture transport has been controlled by westerly winds since at least the Eocene, which is supported by other proxy sources, such as evidence of dust transport from Kazakhstan to northwest China in the Oligocene (Sun et al., 2010). Overall, the observation of steeper longitudinal $\delta^{18}O$ gradients during periods of high pCO_2 points to a past higher P/ET ratio relative to the modern and overall greater net rainout across the continent. This higher paleo-P/ET ratio could reflect either an increase in P during past warm periods, a decrease in ET (perhaps due to changes in transpiration), or some combination of these two factors.

The $\delta^{13}C$ results provide a complementary perspective to shifts in paleoclimate and hydroclimate across Eurasia. These results illustrate an increase in aridity in Asia concurrent with potential increased primary productivity in Europe through the Cenozoic. Although the extent to which the decrease in European $\delta^{13}C$ is driven by the progressive decline in atmospheric pCO_2 or by an increase in primary productivity is not clear, Europe has remained highly productive (relative to northern Asia). It is interesting that major shifts in the $\delta^{13}C$ in Asia are not mirrored in the $\delta^{18}O$ record; that is, changes in primary productivity and aridity appear to have minor influence on the oxygen isotope gradient. There is a slight decrease in the $\delta^{18}O$ in Asia during the latter part of the Cenozoic, which perhaps reflects the increase in aridity. A reduction in vegetation (and thus overall transpiration) may have resulted in a higher evaporative fraction of ET, causing air parcels in Asia to be resupplied with recycled moisture with proportionately more ^{16}O. This slight decrease, however, is not sufficient to substantially steepen the isotopic gradient that shallowed because of the large decrease in $\delta^{18}O$ in Europe. Perhaps the seemingly minor influence of aridity on the $\delta^{18}O$ isotopic gradient in Asia is because nearly all of the moisture that precipitates over Asia is returned to the atmosphere via ET, so the ratio of P/ET is roughly unchanged (~1) throughout the entire Cenozoic. Improved understanding of the evolution of the gradient to varying climate parameters along the transect may help to constrain the shape of the profile in the past and hence more accurately compare the shape of the profile produced by proxy data with modeled gradients.

Comparison of the proxy and model results also inform us of the predictive capacity of both simple and complex models to changes in the terrestrial water cycle with increased atmospheric pCO_2. The shallow gradient under high pCO_2 produced by both the simple reactive transport model and complex isotope-enabled model is likely driven by the faster increase of precipitable water relative to precipitation in warmer climates (Fig. A3). The discrepancy between

the response of the proxy and model gradients to changes in pCO_2 may result from misinterpretation of proxy data, over-prediction of transpiration, and/or underestimating the P/ET ratio under warm conditions. Given the significant effect of vegetation on the terrestrial water cycle in response to increased pCO_2, it is critical to study the continental-scale water and carbon cycles as an interconnected system to accurately model shifts in hydroclimate under future warming. Improved understanding of the response of the critical parameters of P, ET, and q will be vital in projecting future freshwater resources, and better understanding of different proxy biases will help to determine whether there is a true discrepancy between the hydrologic cycle in the past and in models.

Conclusions

We present a compilation of nearly 15,000 stable isotope samples from authigenic carbonate and tooth enamel from Eurasia over the Cenozoic Era to investigate the hydroclimate response to changing paleogeography and atmospheric pCO_2. We use longitudinal gradients of $\delta^{18}O$ to reconstruct moisture transport via the westerlies and investigate how the critical parameters of P, ET, and q respond to higher atmospheric pCO_2. The $\delta^{13}C$ record is utilized to estimate changes in past soil respiration, which in turn informs us of shifts in aridity and primary productivity. The oxygen isotope record demonstrates that the $\delta^{18}O$ in Europe has decreased, likely as a function of shifts in carbonate formation seasonality or changes in the strength of the westerlies, while the $\delta^{18}O$ in Asia has remained stable through the Cenozoic. We also find that westerlies have been the dominant mode of moisture transport across Eurasia since at least the Eocene, given the persistence of a west-to-east isotopic gradient. The $\delta^{13}C$ results suggest an increase in aridity in Asia synchronous with either stable or increased primary productivity in Europe. In summary, the stable isotope record indicates that changes in paleogeography, though quite dramatic in the Cenozoic in both Europe and Asia, do not have a major control on continental-scale moisture transport and hydroclimate across Eurasia. Rather, declining CO_2 and the subsequent effect of global cooling throughout the Cenozoic appears to regulate moisture transport, indicated by shifting seasonality of proxy formation and position of the westerlies.

Additionally, we find that isotopic gradients constructed by both the simple reactive transport model and more complex iCESM fail to align with the reconstructed proxy longitudinal $\delta^{18}O$ gradients, likely due to either a misrepresentation of hydrological variables in these models or to differential changes in authigenic carbonate formation. This work highlights the importance

of understanding the response of vegetation to elevated pCO_2 to predict the availability of future freshwater resources and moisture transport in a warmer climate. Ultimately, collection and compilation of additional proxy samples in regions of Eurasia with sparse data distribution (*i.e.,* central Eurasia) will be crucial to better constrain the proxy gradients and in turn more accurately assess the legitimacy of the model gradients.

Table 1. Model parameters used to run the reactive transport model and data sources for each parameter.

Model Parameter	Data Source/Value Used	References
Mean Air Temperature (K)	Modern: NCEP-DOE AMIP-II	Kanamitsu et al., 2002
	PI, 2xCO_2, 4xCO_2: CESM-CMIP6	Danabasoglu, 2019a; 2019b; 2020
PET ($kg/m^2/s$)	Modern: GLEAM	Martens et al., 2017; Miralles et al., 2011
	PI, 2xCO_2, 4xCO_2: CESM-CMIP6	Danabasoglu, 2019a; 2019b; 2020
Wind Speed (m/s)	Modern: NCEP-DOE AMIP-II	Kanamitsu et al., 2002
	PI, 2xCO_2, 4xCO_2: CESM-CMIP6	Danabasoglu, 2019a; 2019b; 2020
Transpiration Fraction of ET (%)	Modern: 64% PI, 2xCO_2, 4xCO_2: 64%	Good et al., 2015
Initial Precipitable Water (kg/m^2)	Modern: NCEP-DOE AMIP-II	Kanamitsu et al., 2002
	PI, 2xCO_2, 4xCO_2: CESM-CMIP6	Danabasoglu, 2019a; 2019b; 2020
Initial Relative Humidity (%)	Modern: NCEP-DOE AMIP-II	Kanamitsu et al., 2002
	PI, 2xCO_2, 4xCO_2: CESM-CMIP6	Danabasoglu, 2019a; 2019b; 2020
Dryness Index (PET/P)	Modern: GLEAM (PET); GPCC (P)	GLEAM: Martens et al., 2017; Miralles et al., 2011 GPCC: Schneider et al., 2018
	PI, 2xCO_2, 4xCO_2: CESM-CMIP6	Danabasoglu, 2019a; 2019b; 2020
Omega	Modern: 2.6 PI, 2xCO_2, 4xCO_2: 2.6	Greve et al., 2015

Table 2. Estimated mean and one standard deviation of paleo-CO_2 concentrations for each geologic epoch (ppm) (Hoenisch, 2021).

	Modern (PI)	Quaternary	Pliocene	Late Miocene	Early Miocene	Oligocene	Eocene
Mean	280	263.42	329.78	312.81	422.71	831.12	861.63
SD	-	62.43	82.90	116.86	146.16	690.17	674.79

Table 3. Averages and standard deviations (SD) of $\delta^{18}O$ in Europe and Asia by epoch of filtered data (<50°E: 47°-55°N; >50°E: 35°-55°N), with p-value from t-test of significant difference between the two populations within a single epoch. All values given in VSMOW (‰) (longitudinal gradient: ‰/°longitude).

Geologic Epoch	Europe $\delta^{18}O$	SD	Asia $\delta^{18}O$	SD	P-value	Gradient
Modern	-9.06	1.61	-11.15	3.20	2.24e-26*	-0.023
Quaternary	-8.84	2.53	-8.89	2.21	0.093	-0.0075
Pliocene	-9.30	0.98	-8.41	1.82	0.075	0.012
Late Miocene	-2.47	3.44	-7.49	1.77	0.0021*	-0.062
Early Miocene	-3.38	3.75	-8.95	1.83	5.00e-04*	-0.065
Oligocene	-3.06	3.93	-9.31	1.91	4.69e-06*	-0.076
Eocene	-2.74	3.21	-7.58	1.80	8.95e-07*	-0.058

*Indicates statistical significance between Europe and Asia isotope populations ($p < 0.05$)

Table 4. Comparison of the $\delta^{18}O$ gradient (<50°E: 47°-55°N; >50°E: 35°-55°N) between neighboring epoch using 1) confidence intervals at which the slope of the gradients are statistically distinct and 2) p-values from t-test of significant difference between neighboring epochs.

Geologic Epoch	Confidence Interval at which Slopes are different	P-value
Modern-Quaternary	99%	0.053
Quaternary-Pliocene	99%	0.087
Pliocene-Late Miocene	99%	0.0005*
Late Miocene-Early Miocene	18%	0.87
Early Miocene-Oligocene	63%	0.47
Oligocene-Eocene	92%	0.26

*Indicates statistical significance of change in the isotope gradient between neighboring epochs ($p < 0.05$)

Table 5. Averages and standard deviations (SD) of $\delta^{13}C$ in Europe and Asia by epoch, with p-value from t-test of significant difference between the two populations within a single epoch. All values given in VPDB (‰) (longitudinal gradient: ‰/°longitude).

Geologic Epoch	Europe $\delta^{13}C$	SD	Asia $\delta^{13}C$	SD	P-value	Gradient
Quaternary	-7.68	2.76	-2.72	2.47	5.8e-07*	0.054
Pliocene	-7.42	2.39	-3.16	2.64	4.8e-04*	0.041
Late Miocene	-8.66	2.4	-4.60	2.18	0.0015*	0.041
Early Miocene	-4.49	2.43	-5.18	-	-	-0.016
Oligocene	-6.52	-	-4.52	1.69	0.17	0.014
Eocene	-5.87	1.16	-4.51	2.55	-	0.0081

*Indicates statistical significance between Europe and Asia isotope populations ($p < 0.05$)

Table 6. Comparison of the $\delta^{13}C$ gradients between neighboring epoch using 1) confidence intervals at which the slope of the gradients are statistically distinct and 2) p-values from t-test of significant difference between preceding epochs.

Geologic Epoch	Confidence Interval at which Slopes are different	P-value
Quaternary-Pliocene	82%	0.45
Pliocene-Late Miocene	1%	0.99
Late Miocene-Early Miocene	99%	0.07
Early Miocene-Oligocene	69%	0.38
Oligocene-Eocene	24%	0.78

*Indicates statistical significance of change in the isotope gradient between neighboring epochs ($p < 0.05$)

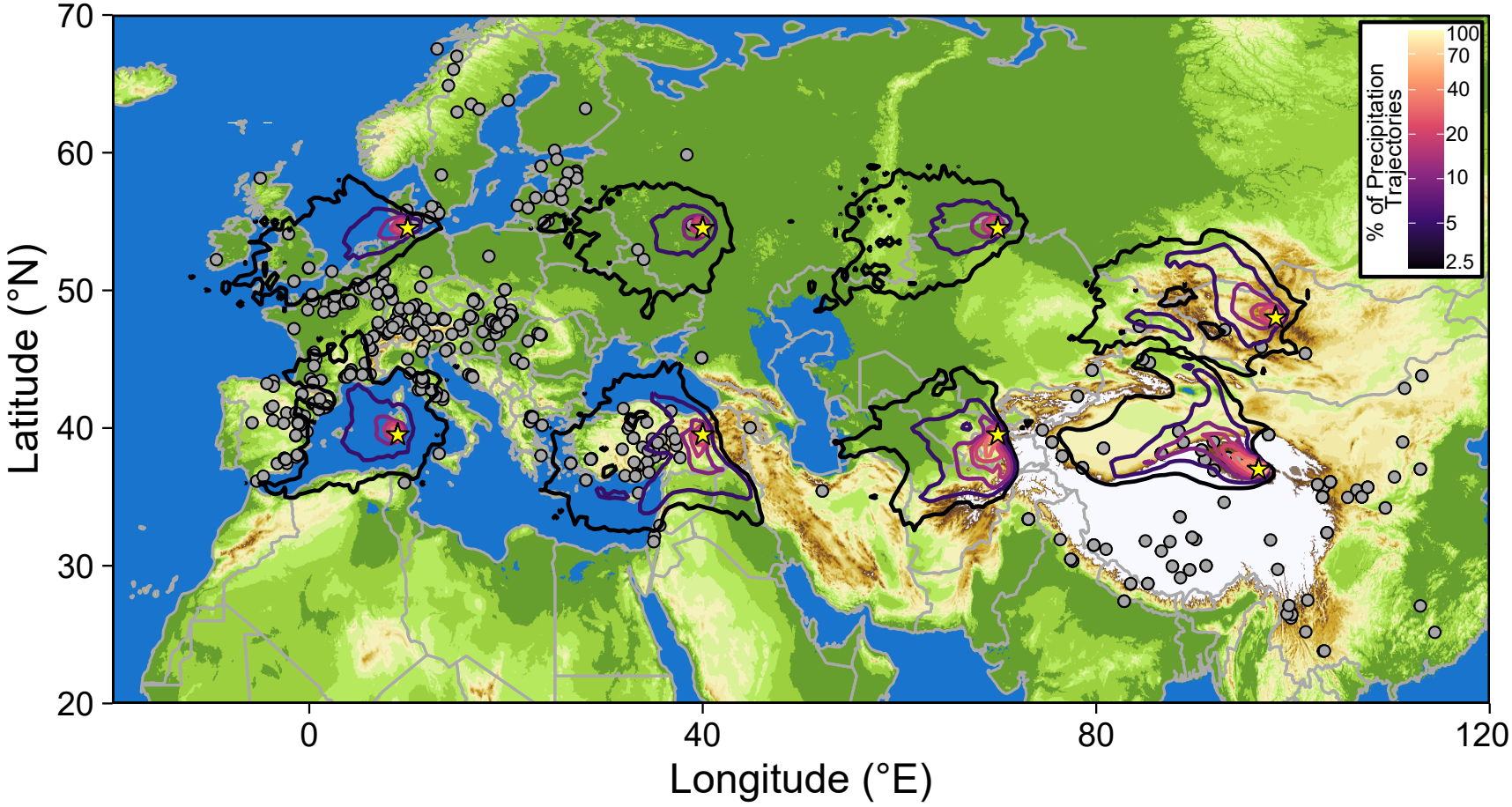

Figure 1. Map of density contours of precipitation-producing air parcel trajectories at eight select locations in Eurasia for 2006-2016 produced using HYSPLIT. Colored lines indicate contours of precipitation-producing trajectory density; dark lines illustrate low density, while lighter tones indicate high density. Yellow stars indicate the starting point of the back-trajectory. Gray points represent all locations of compiled paleo-data. Note that the color scale for contour density is in a log-scale.

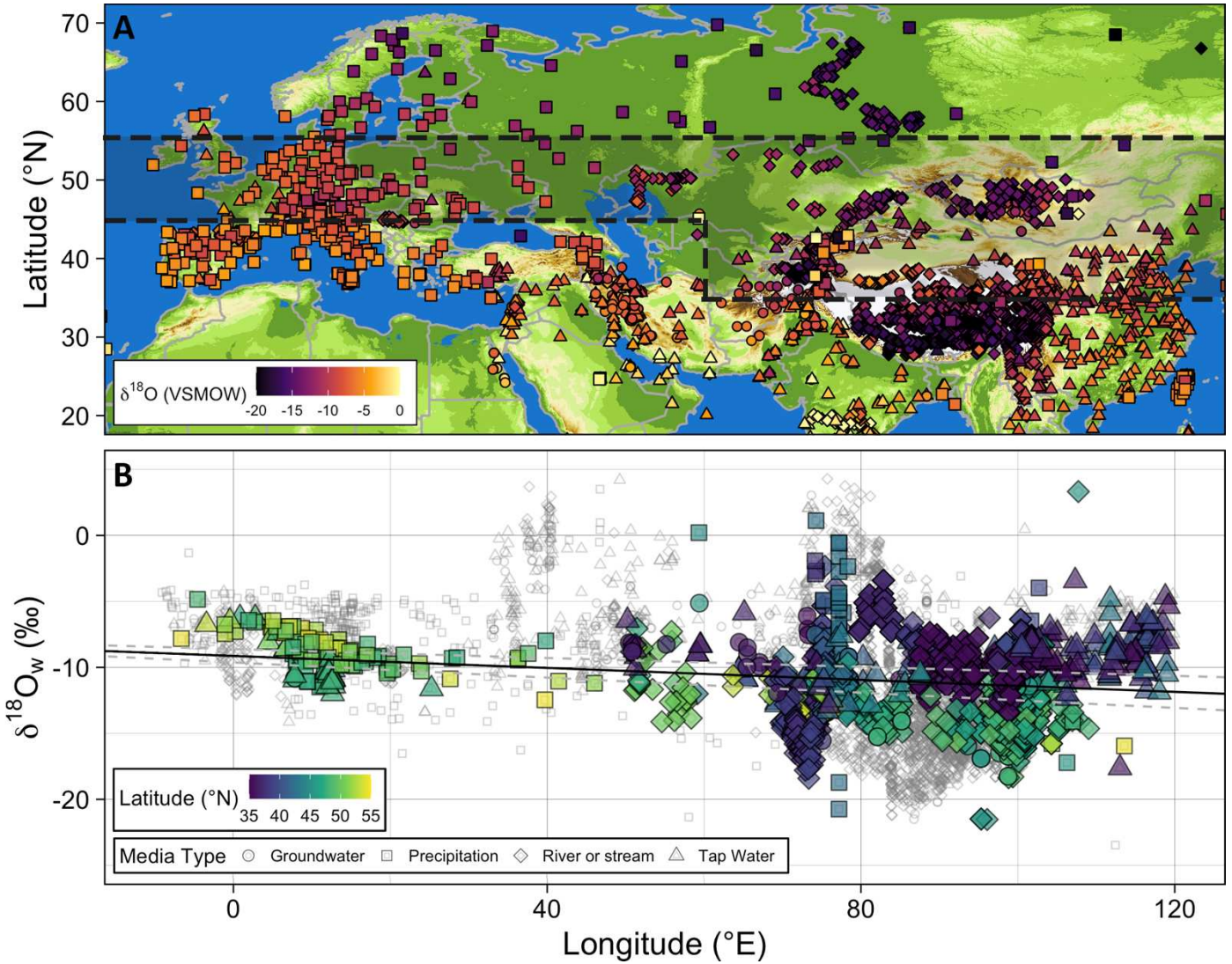

Figure 2A-B. A) Map of compiled annual mean modern $\delta^{18}O$ from groundwater, precipitation, river and stream water, and tap water. Data within dashed lines represent data falling within Atlantic-dominated moisture trajectories ("filtered data", 47°N-55°N in Europe, 35°N-55°N in Asia). B) Longitudinal profile (black line) of the compiled annual mean modern $\delta^{18}O$ gradient, colored by latitude. Dashed lines represent the 95% confidence interval for the profile. Colored and larger points represent "filtered data"; smaller, gray points are all points that fall outside of this range.

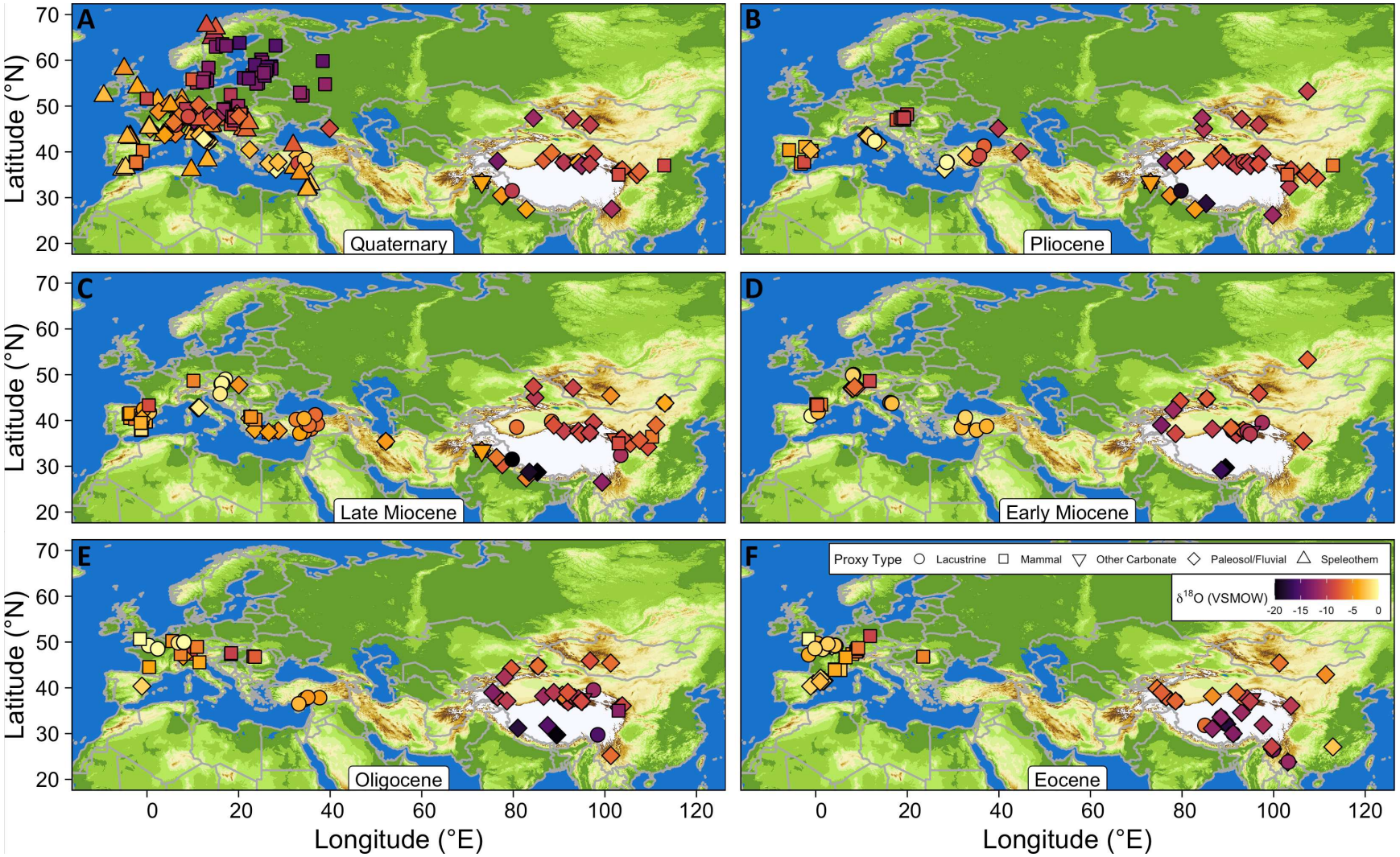

Figure 3A-F. Maps showing spatial distribution of $\delta^{18}O_w$ reconstructed from proxy $\delta^{18}O_{c/e}$ for the Quaternary through the Eocene. $\delta^{18}O_w$ values were reconstructed from $\delta^{18}O_c$ using interpolated surface air temperatures, adjusted for estimated paleotemperatures at time of mineral formation. $\delta^{18}O_w$ was reconstructed from $\delta^{18}O_e$ using mammal-specific equations

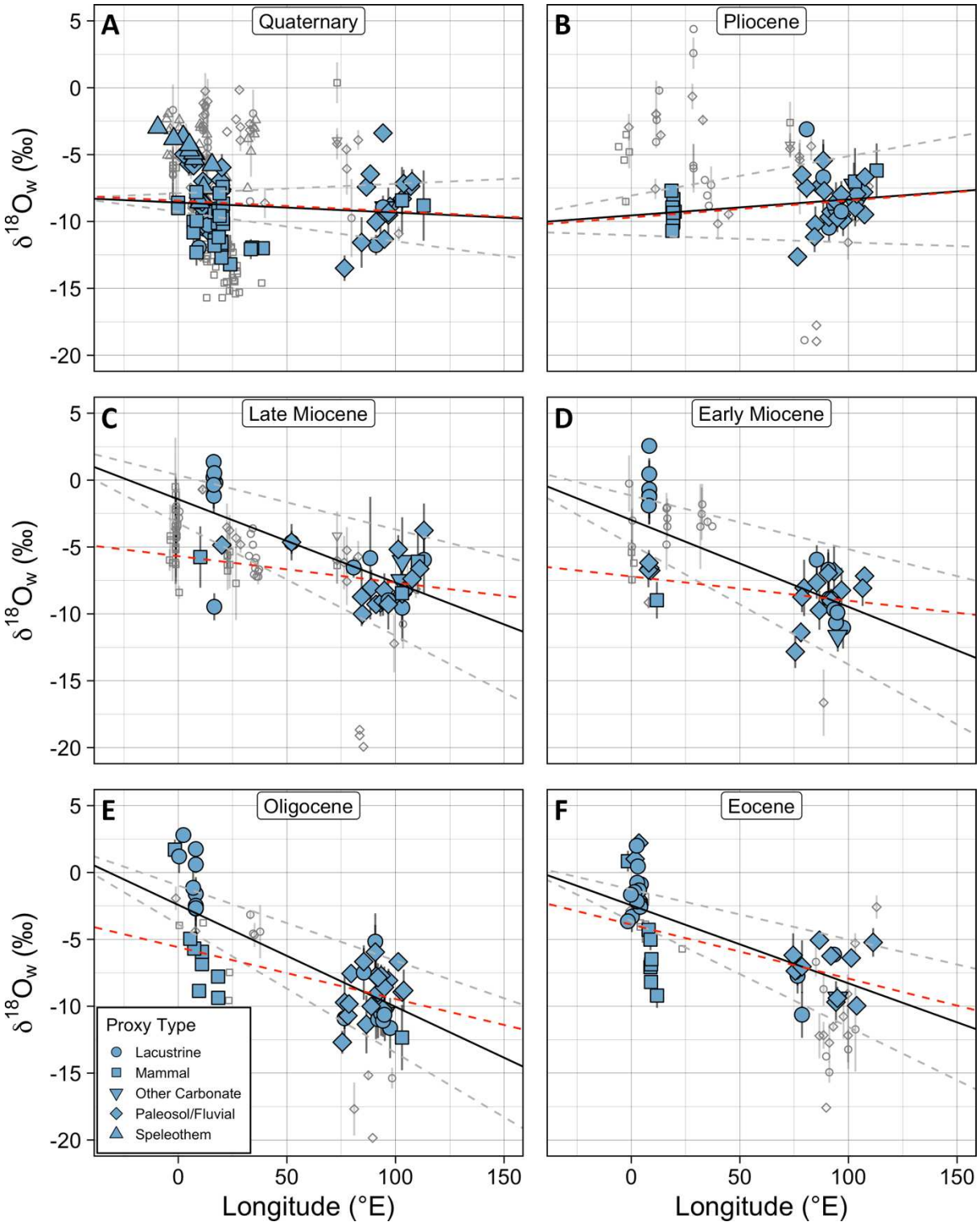

Figure 4A-F. Longitudinal profiles (black lines) of the $\delta^{18}O_w$ gradient reconstructed from proxy $\delta^{18}O_c$ for the Quaternary through the Eocene. Gray dashed lines indicate the 95% confidence interval for the constructed gradients. Red dashed lines show the $\delta^{18}O_w$ gradient without lacustrine proxy data. Colored and larger points represent data falling within Atlantic-dominated moisture trajectories (47°N-55°N in Europe, 35°N-55°N in Asia); smaller, gray points are all points that fall outside of this range.

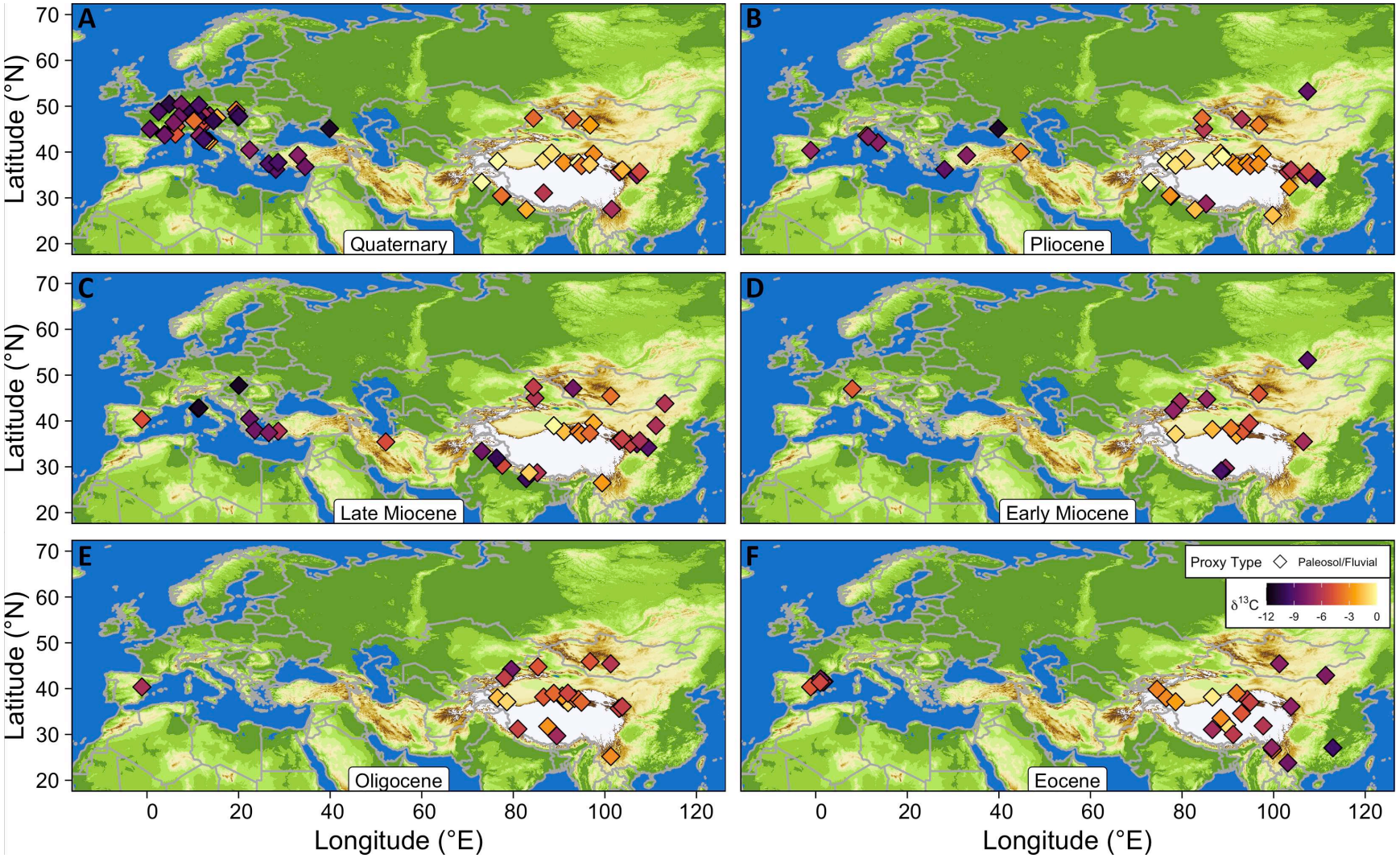

Figure 5A-F. Maps showing spatial distribution of $\delta^{13}C_c$ from paleosol carbonates for the Quaternary through the Eocene across Eurasia.

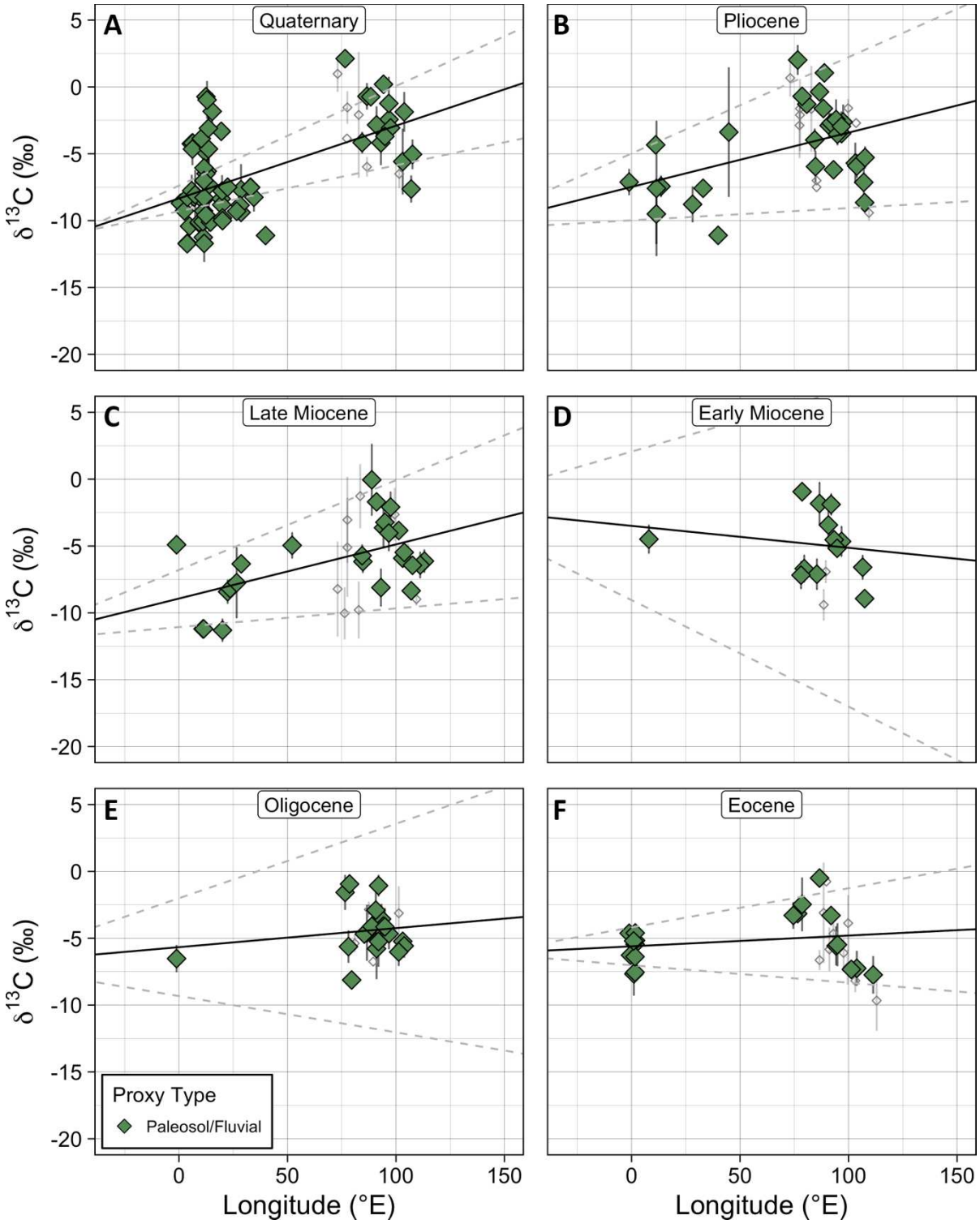

Figure 6A-F. Longitudinal profiles (black lines) of the $\delta^{13}C_c$ gradient for the Quaternary through the Eocene. Dashed lines indicate the 95% confidence interval for the constructed gradients. Colored and larger points represent data falling above reach of the South Asian Monsoon (>35°N in Asia); smaller, gray points are all points that fall outside of this range.

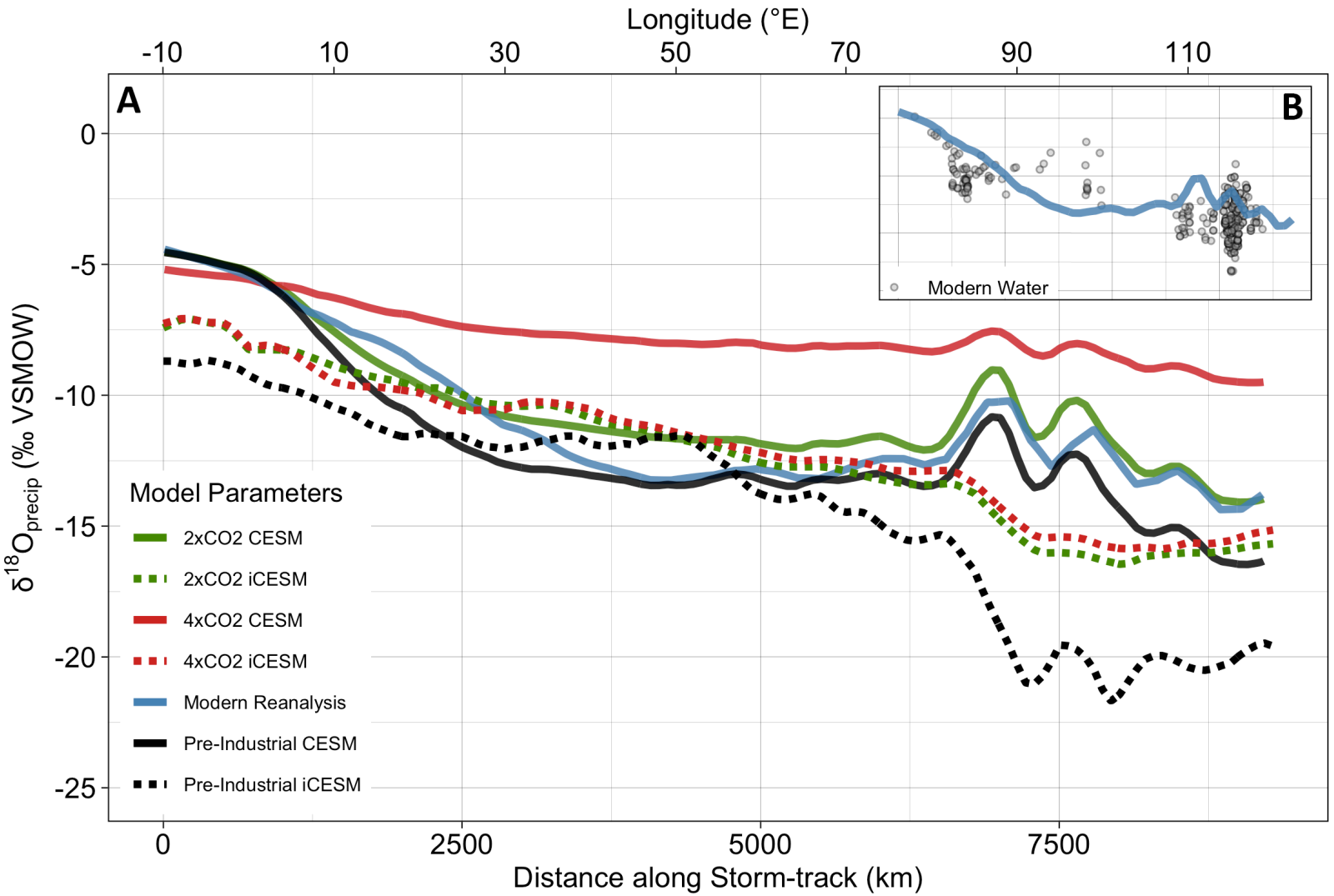

Figure 7A-B. A) Longitudinal $\delta^{18}O_w$ profiles generated using the reactive transport model populated with CESM output at Pre-Industrial CO_2, $2xCO_2$, and $4xCO_2$, and modern reanalysis data (solid lines) to generate predictive proxy gradients at varying pCO_2 concentrations, as well as iCESM $\delta^{18}O_p$ output at Pre-Industrial, $2xCO_2$, and $4xCO_2$ (dashed lines). B) Longitudinal $\delta^{18}O_w$ profile from modern reanalysis output plotted with compiled modern $\delta^{18}O_p$ between 47-50°.

References

Abell, J. T., Winckler, G., Anderson, R. F., & Herbert, T. D. (2021). Poleward and weakened westerlies during Pliocene warmth. Nature, 589(7840), 70–75. https://doi.org/10.1038/s41586-020-03062-1

Abels, H. A., Lauretano, V., Van Yperen, A. E., Hopman, T., Zachos, J. C., Lourens, L. J., Gingerich, P. D., & Bowen, G. J. (2016). Environmental impact and magnitude of paleosol carbonate carbon isotope excursions marking five early Eocene hyperthermals in the Bighorn Basin, Wyoming. Climate of the Past, 12(5), 1151–1163. https://doi.org/10.5194/cp-12-1151-2016

Aggarwal, P. K., Alduchov, O. A., Froehlich, K. O., Araguas-Araguas, L. J., Sturchio, N. C., & Kurita, N. (2012). Stable isotopes in global precipitation: A unified interpretation based on atmospheric moisture residence time. Geophysical Research Letters, 39(11), 1–6. https://doi.org/10.1029/2012GL051937

Ainsworth, E. A., & Rogers, A. (2007). The response of photosynthesis and stomatal conductance to rising [CO 2]: Mechanisms and environmental interactions. Plant, Cell and Environment, 30(3), 258–270. https://doi.org/10.1111/j.1365-3040.2007.01641.x

Amiot, R., Lécuyer, C., Buffetaut, E., Flauteau, F., Legendre, S., and Martineau, F. (2004). Latitudinal temperature gradient during the Cretaceous Upper Campanian-Middle Maastrichtian: $\delta^{18}O$ record of continental vertebrates. Earth and Planetary Science Letters 226, 255-272.

Anagnostou, E., John, E. H., Edgar, K. M., Foster, G. L., Ridgwell, A., Inglis, G. N., Pancost, R. D., Lunt, D. J., & Pearson, P. N. (2016). Changing atmospheric CO_2 concentration was the primary driver of early Cenozoic climate. Nature, 533(7603), 380–384. https://doi.org/10.1038/nature17423

Ao, H., Rohling, E. J., Zhang, R., Roberts, A. P., Holbourn, A. E., Ladant, J. B., Dupont-Nivet, G., Kuhnt, W., Zhang, P., Wu, F., Dekkers, M. J., Liu, Q., Liu, Z., Xu, Y., Poulsen, C. J., Licht, A., Sun, Q., Chiang, J. C. H., Liu, X., … An, Z. (2021). Global warming-induced Asian hydrological climate transition across the Miocene–Pliocene boundary. Nature Communications, 12(1), 1–13. https://doi.org/10.1038/s41467-021-27054-5

Araguás-Araguás, L., Froehlich, K., & Rozanski, K. (1998). Stable isotope composition of precipitation over southeast Asia. Journal of Geophysical Research Atmospheres, 103(D22), 28721–28742. https://doi.org/10.1029/98JD02582

Badger, M. P. S., Lear, C. H., Pancost, R. D., Foster, G. L., Bailey, T. R., Leng, M. J., & Abels, H. A. (2013). CO_2 drawdown following the middle Miocene expansion of the Antarctic Ice Sheet. Paleoceanography, 28(1), 42–53. https://doi.org/10.1002/palo.20015

Badgley, C., Barry, J. C., Morgan, M. E., Nelson, S. V., Behrensmeyer, A. K., Cerling, T. E., & Pilbeam, D. (2008). Ecological changes in Miocene mammalian record show impact of prolonged climatic forcing. Proceedings of the National Academy of Sciences of the United States of America, 105(34), 12145–12149. https://doi.org/10.1073/pnas.0805592105

Baker, A., Hartmann, A., Duan, W., Hankin, S., Comas-Bru, L., Cuthbert, M. O., Treble, P. C., Banner, J., Genty, D., Baldini, L. M., Bartolomé, M., Moreno, A., Pérez-Mejías, C., & Werner, M. (2019). Global analysis reveals climatic controls on the oxygen isotope composition of cave drip water. Nature Communications, 10(1), 1–7. https://doi.org/10.1038/s41467-019-11027-w

Barcikowska, M. J., Kapnick, S. B., & Feser, F. (2018). Impact of large-scale circulation changes in the North Atlantic sector on the current and future Mediterranean winter hydroclimate. Climate Dynamics, 50(5–6), 2039–2059. https://doi.org/10.1007/s00382-017-3735-5

Batibeniz, F., Ashfaq, M., Önol, B., Turuncoglu, U. U., Mehmood, S., & Evans, K. J. (2020). Identification of major moisture sources across the Mediterranean Basin. Climate Dynamics, 54(9–10), 4109–4127. https://doi.org/10.1007/s00382-020-05224-3

Beck, H. E., Zimmermann, N. E., McVicar, T. R., Vergopolan, N., Berg, A., & Wood, E. F. (2018). Present and future köppen-geiger climate classification maps at 1-km resolution. Scientific Data, 5, 1–12. https://doi.org/10.1038/sdata.2018.214

Beerling, D. J., & Royer, D. L. (2011). Convergent Cenozoic CO_2 history. Nature Geoscience, 4(7), 418–420. https://doi.org/10.1038/ngeo1186

Benedict, I., van Heerwaarden, C. C., van der Linden, E. C., Weerts, A. H., & Hazeleger, W. (2021). Anomalous moisture sources of the Rhine basin during the extremely dry summers of 2003 and 2018. Weather and Climate Extremes, 31, 100302. https://doi.org/10.1016/j.wace.2020.100302

Berg, A., & Sheffield, J. (2019). Evapotranspiration partitioning in CMIP5 models: Uncertainties and future projections. Journal of Climate, 32(10), 2653–2671. https://doi.org/10.1175/JCLI-D-18-0583.1

Bialik, O. M., Frank, M., Betzler, C., Zammit, R., & Waldmann, N. D. (2019). Two-step closure of the Miocene Indian Ocean Gateway to the Mediterranean. Scientific Reports, 9(1), 1–10. https://doi.org/10.1038/s41598-019-45308-7

Bisselink, B., & Dolman, A. J. (2008). Precipitation recycling: Moisture sources over Europe using ERA-40 data. Journal of Hydrometeorology, 9(5), 1073–1083. https://doi.org/10.1175/2008JHM962.1

Blumenthal, S. A., Cerling, T. E., Chritz, K. L., Bromage, T. G., Kozdon, R., & Valley, J. W. (2014). Stable isotope time-series in mammalian teeth: In situ $\delta^{18}O$ from the innermost enamel layer. Geochimica et Cosmochimica Acta, 124, 223–236. https://doi.org/10.1016/j.gca.2013.09.032

Bond-Lamberty, B., & Thomson, A. (2010). A global database of soil respiration data. Biogeosciences, 7(6), 1915–1926. https://doi.org/10.5194/bg-7-1915-2010

Botsyun, S., Sepulchre, P., Donnadieu, Y., Risi, C., Licht, A., & Caves Rugenstein, J. K. (2019). Revised paleoaltimetry data show low Tibetan Plateau elevation during the Eocene. Science, 363(6430). https://doi.org/10.1126/science.aaq1436

Bradshaw, C. D., Lunt, D. J., Flecker, R., Salzmann, U., Pound, M. J., Haywood, A. M., & Eronen, J. T. (2012). The relative roles of CO_2 and palaeogeography in determining late Miocene climate: Results from a terrestrial model-data comparison. Climate of the Past, 8(4), 1257–1285. https://doi.org/10.5194/cp-8-1257-2012

Brady, E., Stevenson, S., Bailey, D., Liu, Z., Noone, D., Nusbaumer, J., Otto-Bliesner, B. L., Tabor, C., Tomas, R., Wong, T., Zhang, J., & Zhu, J. (2019). The connected isotopic water cycle in the community earth system model version 1. Journal of Advances in Modeling Earth Systems, 11(8), 2547-2566. https://doi.org/10.1029/2019ms001663

Breecker, D. O., Sharp, Z. D., & McFadden, L. D. (2009). Seasonal bias in the formation and stable isotopic composition of pedogenic carbonate in modern soils from central New Mexico, USA. Bulletin of the Geological Society of America, 121(3–4), 630–640. https://doi.org/10.1130/B26413.1

Breecker, D. O., Sharp, Z. D., & McFadden, L. D. (2010). Atmospheric CO_2 concentrations during ancient greenhouse climates were similar to those predicted for A.D. 2100. Proceedings of the National Academy of Sciences of the United States of America, 107(2), 576–580. https://doi.org/10.1073/pnas.0902323106

Brittingham, A., Petrosyan, Z., Hepburn, J. C., Richards, M. P., Hren, M. T., & Hartman, G. (2019). Influence of the North Atlantic Oscillation on δD and $\delta^{18}O$ in meteoric water in the Armenian Highland. Journal of Hydrology, 575(November 2018), 513–522. https://doi.org/10.1016/j.jhydrol.2019.05.064

Broccoli, A. J., & Manabe, S. (1992). The Effects of Orography on Midlatitude Northern Hemisphere Dry Climates. Journal of Climate, 5, 1181–1201.

Brönnimann, S., Rajczak, J., Fischer, E., Raible, C., Rohrer, M., & Schär, C. (2018). Changing seasonality of moderate and extreme precipitation events in the Alps. Natural Hazards and Earth System Sciences, 18(7), 2047–2056. https://doi.org/10.5194/nhess-18-2047-2018

Budyko, M. I. (1974). Climate and life. New York: Academic Press.

Burgener, L., Hyland, E., Huntington, K. W., Kelson, J. R., & Sewall, J. O. (2019). Revisiting the equable climate problem during the Late Cretaceous greenhouse using paleosol carbonate clumped isotope temperatures from the Campanian of the Western Interior Basin, USA. Palaeogeography, Palaeoclimatology, Palaeoecology, 516(December 2018), 244–267. https://doi.org/10.1016/j.palaeo.2018.12.004

Campani, M., Mulch, A., Kempf, O., Schlunegger, F., & Mancktelow, N. (2012). Miocene paleotopography of the Central Alps. Earth and Planetary Science Letters, 337–338, 174–185. https://doi.org/10.1016/j.epsl.2012.05.017

Caves, J. K., Winnick, M. J., Graham, S. A., Sjostrom, D. J., Mulch, A., & Chamberlain, C. P. (2015). Role of the westerlies in Central Asia climate over the Cenozoic. *Earth and* Planetary Science Letters, 428(October), 33–43. https://doi.org/10.1016/j.epsl.2015.07.023

Caves, J. K., Moragne, D. Y., Ibarra, D. E., Bayshashov, B. U., Gao, Y., Jones, M. M., Zhamangara, A., Arzhannikova, A. V., Arzhannikov, S. G., & Chamberlain, C. P. (2016). The Neogene de-greening of Central Asia. Geology, 44(11), 887–890. https://doi.org/10.1130/G38267.1

Celle-Jeanton, H., Travi, Y., & Blavoux, B. (2001). Isotopic typology of the precipitation in the Western Mediterranean region at the three different time scales. *Geophysical Research Letters*, *28*(7), 1215–1218. https://doi.org/10.1029/2000GL012407

Cerling, T. E. (1984). The stable isotopic composition of modern soil carbonate and its relationship to climate. Earth and Planetary Science Letters, 71, 229–240.

Cerling, T. E. (1991). Carbon dioxide in the atmosphere; evidence from Cenozoic and Mesozoic Paleosols. American Journal of Science, 291(4), 377–400. https://doi.org/10.2475/ajs.291.4.377

Cerling, T. E. (1999). Paleorecords of C4 Plants and Ecosystems. In *C4 Plant Biology*. Woodhead Publishing Limited. https://doi.org/10.1016/b978-012614440-6/50014-8

Cerling, T. E., Harris, J. M., MacFadden, B. J., Leakey, M. G., Quade, J., Eisenmann, V., & Ehieringer, J. R. (1997). Global vegetation change through the Miocene/Pliocene boundary. Nature, 389(6647), 153–158. https://doi.org/10.1038/38229

Cheng, T. F., Lu, M., & Dai, L. (2021). Moisture channels and pre-existing weather systems for East Asian rain belts. Npj Climate and Atmospheric Science, 4(1), 1–13. https://doi.org/10.1038/s41612-021-00187-6

Cohen, J., Cohen, P., West, S.G., & Aiken, L.S. (2003). Applied Multiple Regression/Correlation Analysis for the Behavioral Sciences (3rd edition). Mahwah, NJ: Lawrence Earlbaum Associates.

Computational and Information Systems Laboratory (2019). Cheyenne: HPE/SGI ICE XA System (Climate Simulation Laboratory). Boulder, CO: National Center for Atmospheric Research. https://doi.org/10.5065/D6RX99HX

Cyr, A.J., Currie, B.S., & Rowley, D.B. (2005). Geochemical Evaluation of Fenghuishan Group Lacustrine Carbonates, North-Central Tibet: Implications for the Paleoaltimetry of the Eocene Tibetan Plateau. The Journal of Geology, 113, 517-533.

Danabasoglu, G. (2019a). NCAR CESM2 model output prepared for CMIP6 CMIP ESM-piControl. Version 20190320. Earth System Grid Federation. https://doi.org/10.22033/ESGF/CMIP6.7579

Danabasoglu, G. (2019b). NCAR CESM2 model output prepared for CMIP6 CMIP abrupt-4xCO_2. Version 20200408. Earth System Grid Federation. https://doi.org/10.22033/ESGF/CMIP6.7518

Danabasoglu, G. (2020). NCAR CESM2 model output prepared for CMIP6 CFMIP abrupt-2xCO_2. Version 20190927. Earth System Grid Federation. https://doi.org/10.22033/ESGF/CMIP6.7519

DeCelles, P. G., Kapp, P., Gehrels, G. E., & Ding, L. (2014). Paleocene-Eocene foreland basin evolution in the Himalaya of southern Tibet and Nepal: Implications for the age of initial India-Asia collision. Tectonics, 33(5), 824–849. https://doi.org/10.1002/2014TC003522

Dee, D. P., Uppala, S. M., Simmons, A. J., Berrisford, P., Poli, P., Kobayashi, S., Andrae, U., Balmaseda, M. A., Balsamo, G., Bauer, P., Bechtold, P., Beljaars, A. C. M., van de Berg, L., Bidlot, J., Bormann, N., Delsol, C., Dragani, R., Fuentes, M., Geer, A. J., Haimberger, L., Healy, S. B., Hersbach, H., Hólm, E. V., Isaksen, L., Kållberg, P., Köhler, M., Matricardi, M., McNally, A. P., Monge-Sanz, B. M., Morcrette, J. J., Park, B. K., Peubey, C., de Rosnay, P., Tavolato, C., Thépaut, J. N., & Vitart, F. (2011). The ERA-Interim reanalysis: configuration and performance of the data assimilation system. Quarterly Journal of the Royal Meteorological Society, 137, 553–597, https://doi.org/10.1002/qj.828

Diefendorf, A. F., Mueller, K. E., Wing, S. L., Koch, P. L., & Freeman, K. H. (2010). Global patterns in leaf ^{13}C discrimination and implications for studies of past and future climate. Proceedings of the National Academy of Sciences of the United States of America, 107(13), 5738–5743. https://doi.org/10.1073/pnas.0910513107

Dolan, A. M., Haywood, A. M., Hunter, S. J., Tindall, J. C., Dowsett, H. J., Hill, D. J., & Pickering, S. J. (2015). Modelling the enigmatic Late Pliocene Glacial Event - Marine Isotope Stage M2. Global and Planetary Change, 128, 47–60. https://doi.org/10.1016/j.gloplacha.2015.02.001

Domingo, L., Koch, P.L., Fernández, M.H., Fox, D.L., Domingo, M.S., & Alberdi, M.T. (2013). Late Neogene and Early Quaternary Paleoenvironmental and Paleoclimatic Conditions in Southwestern Europe: Isotopic Analyses on Mammalian Taxa. PLOS One, 8(May), 1-15.

Dong, J., Lei, F., & Crow, W. T. (2022). Land transpiration-evaporation partitioning errors responsible for modeled summertime warm bias in the central United States. Nature Communications, 13(1), 1–8. https://doi.org/10.1038/s41467-021-27938-6

Eamus, D., & Jarvis, P. G. (1989). The Direct Effects of Increase in the Global Atmospheric CO_2 Concentration on Natural and Commercial Temperate Trees and Forests. Advances in Ecological Research, 19, 1–58. https://doi.org/10.1016/S0065-2504(03)34001-2

Edwards, E. J., Osborne, C. P., Strömberg, C. A. E., Smith, S. A., & C4 Grasses Consortium. (2010). The origins of C4 grasslands: integrating evolutionary and ecosystem science. Science, 328, 587–59.

Ehleringer, J. R., Buchmann, N., & Flanagan, L. B. (2000). Carbon isotope ratios in belowground carbon cycle processes. Ecological Applications, 10(2), 412–422. https://doi.org/10.1890/1051-0761(2000)010[0412:CIRIBC]2.0.CO;2

Eyring, V., Bony, S., Meehl, G.A., Senior, C.A., Stevens, B., Stouffer, R.J., & Taylor, K.E. (2016). Overview of the Coupled Model Intercomparison Project Phase 6 (CMIP6) experimental design and organization. Geoscientific Model Development, 9(5), 1937-1958. https://doi.org/10.5194/gmd-9-1937-2016

Findell, K. L., Keys, P. W., van der Ent, R. J., Lintner, B. R., Berg, A., & Krasting, J. P. (2019). Rising temperatures increase importance of oceanic evaporation as a source for continental precipitation. Journal of Climate, 32(22), 7713–7726. https://doi.org/10.1175/JCLI-D-19-0145.1

Fricke, H. C., Rogers, R. R., & Gates, T. A. (2009). Hadrosaurid migration: inferences based on stable isotope comparisons among Late Cretaceous dinosaur localities. Paleobiology, 35(2), 270–288. https://doi.org/10.1666/08025.1

Gangoiti, G., Sáez de Cámara, E., Alonso, L., Iza, J., García, J. A., Valdenebro, V., Gómez, M. C., Navazo, M., & García, E. (2020). Simultaneous Episodes of Heavy Rainfall in Morocco and Southern Alps: 2. Time Scales and Mapping of Remote and Local Evaporative Sources. Journal of Geophysical Research: Atmospheres, 125(4), 1–30. https://doi.org/10.1029/2019JD030437

Garzione, C. N., Dettman, D. L., & Horton, B. K. (2004). Carbonate oxygen isotope paleoaltimetry: evaluating the effect of diagenesis on paleoelevation estimates for the Tibetan plateau. Palaeogeography, Palaeoclimatology, Palaeoecology, 212(1–2), 119–140. https://doi.org/10.1016/j.palaeo.2004.05.020

GLEAM v3.5a , last accessed from www.GLEAM.eu on March 15 2021, provided with transposed coordinates as daily / monthly files comprising all parameters by the Integrated Climate Data Center (ICDC),CEN, University of Hamburg.

Greve, P., Gudmundsson, L., Orlowsky, B., & Seneviratne, S. I. (2015). Introducing a probabilistic Budyko framework. Geophysical Research Letters, 42(7), 2261–2269. https://doi.org/10.1002/2015GL063449

Greve, P., Orlowsky, B., Mueller, B., Sheffield, J., Reichstein, M., and Senevirante, S.I. (2014). Global assessment of trends in wetting and drying over land. Nature Geoscience, 7(10), 716-721. https://doi.org/10.1038/NGEO2247.

Good, S. P., Noone, D., & Bowen, G. (2015). Hydrologic connectivity constrains partitioning of global terrestrial water fluxes. Science, 349(6244), 175–177. https://doi.org/10.1126/science.aaa5931

Hamon, N., Sepulchre, P., Lefebvre, V., & Ramstein, G. (2013). The role of eastern Tethys seaway closure in the Middle Miocene Climatic Transition (ca. 14 Ma). Climate of the Past, 9(6), 2687–2702. https://doi.org/10.5194/cp-9-2687-2013

Handy, M. R., M. Schmid, S., Bousquet, R., Kissling, E., & Bernoulli, D. (2010). Reconciling plate-tectonic reconstructions of Alpine Tethys with the geological-geophysical record of spreading and subduction in the Alps. Earth-Science Reviews, 102(3–4), 121–158. https://doi.org/10.1016/j.earscirev.2010.06.002

Haug, G. H., & Tiedemann, R. (1998). Effect of the formation of the Isthmus of Panama on Atlantic Ocean thermohaline circulation. Letters to Nature, 393, 673–676.

Hayashi, T., Yamanaka, T., Hikasa, Y., Sato, M., Kuwahara, Y., & Ohno, M. (2020). Latest Pliocene Northern Hemisphere glaciation amplified by intensified Atlantic meridional overturning circulation. Communications Earth & Environment, 1(1), 4–5. https://doi.org/10.1038/s43247-020-00023-4

Held, I. M., & Soden, B. J. (2006). Robust responses of the hydrological cycle to global warming. Journal of Climate, 19(21), 5686–5699. https://doi.org/10.1175/JCLI-D-18-0238.1

Herold, N., Huber, M., Greenwood, D. R., Müller, R. D., & Seton, M. (2011). Early to middle Miocene monsoon climate in Australia. Geology, 39(1), 3–6. https://doi.org/10.1130/G31208.1

Hoenisch, B. (2021). Paleo-CO2 data archive (Version 1) [Data set]. Zenodo. https://doi.org/10.5281/zenodo.5777278

Holbourn, A., Kuhnt, W., Schulz, M., Flores, J. A., & Andersen, N. (2007). Orbitally-paced climate evolution during the middle Miocene "Monterey" carbon-isotope excursion. Earth and Planetary Science Letters, 261(3–4), 534–550. https://doi.org/10.1016/j.epsl.2007.07.026

Horton, T. W., Defliese, W. F., Tripati, A. K., & Oze, C. (2016). Evaporation induced ^{18}O and ^{13}C enrichment in lake systems: A global perspective on hydrologic balance effects. Quaternary Science Reviews, 131, 365–379. https://doi.org/10.1016/j.quascirev.2015.06.030

Hurrell, J. W., & Van Loon, H. (1997). Decadal variations in climate associated with the North Atlantic oscillation. Climatic Change, 36(3–4), 301–326. https://doi.org/10.1023/a:1005314315270

Huth, T. E., Cerling, T. E., Marchetti, D. W., Bowling, D. R., Ellwein, A. L., & Passey, B. H. (2019). Seasonal Bias in Soil Carbonate Formation and Its Implications for Interpreting High-Resolution Paleoarchives: Evidence from Southern Utah. Journal of Geophysical Research: Biogeosciences, 124(3), 616–632. https://doi.org/10.1029/2018JG004496

Huyghe, D., Mouthereau, F., Sébilo, M., Vacherat, A., Ségalen, L., Richard, P., Biron, P., & Bariac, T. (2018). Impact of topography, climate and moisture sources on isotopic composition ($\delta^{18}O$ & δD) of rivers in the Pyrenees: Implications for topographic reconstructions in small orogens. Earth and Planetary Science Letters, 484, 370–384. https://doi.org/10.1016/j.epsl.2017.12.035

IAEA 2020. Global Network of Isotopes in Rivers. The GNIR Database. Accessible at: https://nucleus.iaea.org/wiser.

IAEA/WMO 2020. Global Network of Isotopes in Precipitation. The GNIP Database. Accessible at: https://nucelus.iaea.org/wiser.

Ibarra, D. E., Oster, J. L., Winnick, M. J., Rugenstein, J. K. C., Byrne, M. P., & Chamberlain, C. P. (2018). Warm and cold wet states in the western United States during the Pliocene-Pleistocene. Geology, 46(4), 355–358. https://doi.org/10.1130/G39962.1

James, E.W., Banner, J.L., & Hardt, B. (2015). A global model for cave ventilation and seasonal bias in speleothem paleoclimate records. Geochemistry, Geophysics, Geosystems, 16, 1044-1051.

Jung, M., Reichstein, M., Margolis, H. A., Cescatti, A., Richardson, A. D., Arain, M. A., Arneth, A., Bernhofer, C., Bonal, D., Chen, J., Gianelle, D., Gobron, N., Kiely, G., Kutsch, W., Lasslop, G., Law, B. E., Lindroth, A., Merbold, L., Montagnani, L., … Williams, C. (2011). Global patterns of land-atmosphere fluxes of carbon dioxide, latent heat, and sensible heat derived from eddy covariance, satellite, and meteorological observations. Journal of Geophysical Research: Biogeosciences, 116(3), 1–16. https://doi.org/10.1029/2010JG001566

Kanamitsu, M., Ebisuzaki, W., Woollen, J., Yang, S-K., Hnilo, J.J., Fiorino, M., and Potter, G.L. (2002), NCEP-DOE AMIP-II Reanalysis (R-2), Bulletin of the American Meteorological Society, v.83, p. 1631-1644

Katul, G. G., Oren, R., Manzoni, S., Higgins, C., & Parlange, M. B. (2012). Evapotranspiration: A process driving mass transport and energy exchange in the soil-plant-atmosphere-climate system. Reviews of Geophysics, 50(3). https://doi.org/10.1029/2011RG000366

Kelemen, F. D., Ludwig, P., Reyers, M., Ulbrich, S., & Pinto, J. G. (2016). Evaluation of moisture sources for the Central European summer flood of May/June 2013 based on regional climate model simulations. Tellus, Series A: Dynamic Meteorology and Oceanography, 68(June 2013). https://doi.org/10.3402/tellusa.v68.29288

Keys, P., Barron, J., & Lannerstad, M. (2012). Releasing the Pressure: Water Resource Efficiencies and Gains for Ecosystems Services. Nairobi: United Nations Environment Programme, and Stockholm: Stockholm Environment Institute.

Keys, P. W., & Wang-Erlandsson, L. (2018). On the social dynamics of moisture recycling. Earth System Dynamics, 9(2), 829–847. https://doi.org/10.5194/esd-9-829-2018

Keys, P. W., Wang-Erlandsson, L., & Gordon, L. J. (2018). Megacity precipitationsheds reveal teleconnected water security challenges. PLOS One, 13(3), 1–22. https://doi.org/10.1371/journal. pone.0194311

Kim, S. T., & O'Neil, J. R. (1997). Equilibrium and nonequilibrium oxygen isotope effects in synthetic carbonates. Geochimica et Cosmochimica Acta, 61(16), 3461–3475. https://doi.org/10.1016/S0016-7037(97)00169-5

Kimball, B. A., Mauney, J. R., Nakayama, F. S., & Idso, S. B. (1993). Effects of increasing atmospheric CO_2 on vegetation. Vegetatio, 104–105(1), 65–75. https://doi.org/10.1007/BF00048145

Kirschbaum, M. U. F., & McMillan, A. M. S. (2018). Warming and Elevated CO_2 Have Opposing Influences on Transpiration. Which is more Important? Current Forestry Reports, 4(2), 51–71. https://doi.org/10.1007/s40725-018-0073-8

Knorr, G., Butzin, M., Micheels, A., & Lohmann, G. (2011). A warm Miocene climate at low atmospheric CO_2 levels. Geophysical Research Letters, 38(20), 1–5. https://doi.org/10.1029/2011GL048873

Koch, P. (2007). Isotopic study of the biology of modern and fossil vertebrates. In R.H. Michener, and K. Lajtha (Eds.), *Stable Isotopes in Ecology and Environmental Science*. Second edition. Malden, MA: Blackwell Publishing, 2007.

Kohn, M. J. (1996). Predicting animal $\delta^{18}O$: Accounting for diet and physiological adaptation. Geochimica et Cosmochimica Acta, 60(23), 4811–4829. https://doi.org/10.1016/S00167037(96)00240-2

Kohn, M. J. (2004). Comment: Tooth enamel mineralization in ungulates: Implications for recovering a primary isotopic time-series, by B. H. Passey and T. E. Cerling (2002). Geochimica et Cosmochimica Acta, 68(2), 403–405. https://doi.org/10.1016/S0016-7037(03)00443-5

Kohn, M. J. (2010). Carbon isotope compositions of terrestrial C3 plants as indicators of (paleo)ecology and (paleo)climate. Proceedings of the National Academy of Sciences of the United States of America, 107(46), 19691–19695. https://doi.org/10.1073/pnas.1004933107

Kohn, M. J., & Law, J. M. (2006). Stable isotope chemistry of fossil bone as a new paleoclimate indicator. Geochimica et Cosmochimica Acta, 70(4), 931–946. https://doi.org/10.1016/j.gca.2005.10.023

Kohn, M. J., & Cerling, T. E. (2019). Stable isotope compositions of biological apatite. Phosphates: Geochemical, Geobiological and Materials Importance, 48(McCrea 1950), 455–488. https://doi.org/10.2138/rmg.2002.48.12

Krsnik, E., Methner, K., Campani, M., Botsyun, S., Mutz, S. G., Ehlers, T. A., Kempf, O., Fiebig, J., Schlunegger, F., & Mulch, A. (2021). Miocene high elevation in the Central Alps. Solid Earth, 12(11), 2615–2631. https://doi.org/10.5194/se-12-2615-2021

Kukla, T., Winnick, M. J., Maher, K., Ibarra, D. E., & Chamberlain, C. P. (2019). The Sensitivity of Terrestrial $\delta^{18}O$ Gradients to Hydroclimate Evolution. Journal of Geophysical Research: Atmospheres, 124(2), 563–582. https://doi.org/10.1029/2018JD029571

Kukla, T., Rugenstein, J. K. C., & Driscoll, E. (2022a). The PATCH (Paleo Analysis of Terrestrial Climate and Hydrology) Lab - A database and workspace. The PATCH Lab. Retrieved 2022, from https://geocentroid.shinyapps.io/PATCH-Lab/

Kukla, T., Rugenstein, J. K. C., Ibarra, D. E., Winnick, M. J., Strömberg, C. A. E., & Chamberlain, C. P. (2022b). Drier Winters Drove Cenozoic Open Habitat Expansion in North America. AGU Advances, 3(2), 1–20. https://doi.org/10.1029/2021av000566

Kukla, T., Rugenstein, J., Driscoll, E., Ibarra, D.E., & Chamberlain, C.P. (in review). The PATCH Lab: A database and workspace for Cenozoic terrestrial paleoclimate and environment reconstruction. American Journal of Science.

Kurita, N., Yoshida, N., Inoue, G., & Chayanova, E. A. (2004). Modern isotope climatology of Russia: A first assessment. Journal of Geophysical Research: Atmospheres, 109(3), 1–15. https://doi.org/10.1029/2003jd003404

Lachniet, M. S. (2009). Climatic and environmental controls on speleothem oxygen-isotope values. Quaternary Science Reviews, 28(5–6), 412–432. https://doi.org/10.1016/j.quascirev.2008.10.021

Lawrence, D. M., Oleson, K. W., Flanner, M. G., Fletcher, C. G., Lawrence, P. J., Levis, S., Swenson, S. C., & Bonan, G. B. (2012). The CCSM4 land simulation, 1850-2005: Assessment of surface climate and new capabilities. Journal of Climate, 25(7), 2240–2260. https://doi.org/10.1175/JCLI-D-11-00103.1

Lear, C.H., Elderfield, H., and Wilson, P.A. (2000). Cenozoic Deep-Sea Temperatures and Global Ice Volumes from Mg/Ca in Benthic Foraminiferal Calcite. Sciences, 287, 269-272.

Leipprand, A., & Gerten, D. (2006). Global effects of doubled atmospheric CO_2 content on evapotranspiration, soil moisture and runoff under potential natural vegetation. Hydrological Sciences Journal, 51(1), 171–185. https://doi.org/10.1623/hysj.51.1.171

Lemordant, L., Gentine, P., Swann, A. S., Cook, B. I., & Scheff, J. (2018). Critical impact of vegetation physiology on the continental hydrologic cycle in response to increasing CO_2. Proceedings of the National Academy of Sciences of the United States of America, 115(16), 4093–4098. https://doi.org/10.1073/pnas.1720712115

Leng, M. J., & Marshall, J. D. (2004). Palaeoclimate interpretation of stable isotope data from lake sediment archives. Quaternary Science Reviews, 23(7–8), 811–831. https://doi.org/10.1016/j.quascirev.2003.06.012

Li, J. H., Dugas, W. A., Hymus, G. J., Johnson, D. P., Hinkle, C. R., Drake, B. G., & Hungate, B. A. (2003). Direct and indirect effects of elevated CO_2 on transpiration from Quercus myrtifolia in a scrub-oak ecosystem. Global Change Biology, 9(1), 96–105. https://doi.org/10.1046/j.1365-2486.2003.00557.x

Li, J. X., Yue, L. P., Roberts, A. P., Hirt, A. M., Pan, F., Guo, L., Xu, Y., Xi, R. G., Guo, L., Qiang, X. K., Gai, C. C., Jiang, Z. X., Sun, Z. M., & Liu, Q. S. (2018). Global cooling and enhanced Eocene Asian mid-latitude interior aridity. Nature Communications, 9(1), 1–8. https://doi.org/10.1038/s41467-018-05415-x

Li, L., & Garzione, C. N. (2017). Spatial distribution and controlling factors of stable isotopes in meteoric waters on the Tibetan Plateau: Implications for paleoelevation reconstruction. Earth and Planetary Science Letters, 460, 302–314. https://doi.org/10.1016/j.epsl.2016.11.046

Li, S., Currie, B.S., Rowley, D.B., & Ingalls, M. (2015). Cenozoic paleoaltimetry of the SE margin of the Tibetan Plateau: Constraints on the tectonic evolution of the region. Earth and Planetary Science Letters, 432, 415-424.

Liu, L., Eronen, J. T., & Fortelius, M. (2009). Significant mid-latitude aridity in the middle Miocene of East Asia. Palaeogeography, Palaeoclimatology, Palaeoecology, 279(3–4), 201–206. https://doi.org/10.1016/j.palaeo.2009.05.014

Liu, Z., Bowen, G. J., & Welker, J. M. (2010). Atmospheric circulation is reflected in precipitation isotope gradients over the conterminous United States. Journal of Geophysical Research Atmospheres, 115(22), 1–14. https://doi.org/10.1029/2010JD014175

Lunt, D. J., Foster, G. L., Haywood, A. M., & Stone, E. J. (2008). Late Pliocene Greenland glaciation controlled by a decline in atmospheric CO_2 levels. Nature, 454(7208), 1102–1105. https://doi.org/10.1038/nature07223

Manea, A., & Leishman, M. R. (2015). Competitive interactions between established grasses and woody plant seedlings under elevated CO_2 levels are mediated by soil water availability. Oecologia, 177(2), 499–506. https://doi.org/10.1007/s00442-014-3143-z

Martens, B., Miralles, D. G., Lievens, H., van der Schalie, R., de Jeu, R. A. M., Fernandez-Prieto, D., Beck,H. E., Dorigo, W. A., and Verhoest, N. E. C. (2017), GLEAM v3: satellite-based land evaporation and root-zone soil moisture, Geoscientific Model Development, 10, 1903-1925. https://doi.org/10.5194/gmp-10-1903-2017

Matson, S.D., & Fox, D.L. (2010). Stable isotopic evidence for terrestrial latitudinal climate gradients in the Late Miocene of the Iberian Peninsula. Palaeogeography, Palaeoclimatology, Palaeoecology, 287, 28-44.

McDermott, F., Atkinson, T. C., Fairchild, I. J., Baldini, L. M., & Mattey, D. P. (2011). A first evaluation of the spatial gradients in $\delta^{18}O$ recorded by European Holocene speleothems. Global and Planetary Change, 79(3–4), 275–287. https://doi.org/10.1016/j.gloplacha.2011.01.005

Mejía, L. M., Méndez-Vicente, A., Abrevaya, L., Lawrence, K. T., Ladlow, C., Bolton, C., Cacho, I., & Stoll, H. (2017). A diatom record of CO_2 decline since the late Miocene. Earth and Planetary Science Letters, 479, 18–33. https://doi.org/10.1016/j.epsl.2017.08.034

Methner, K., Campani, M., Fiebig, J., Löffler, N., Kempf, O., & Mulch, A. (2020). Middle Miocene long-term continental temperature change in and out of pace with marine climate records. Scientific Reports, 10(1), 1–10. https://doi.org/10.1038/s41598-020-64743-5

Meulenkamp, J. E., & Sissingh, W. (2003). Tertiary palaeogeography and tectonostratigraphic evolution of the Northern and Southern Peri-Tethys platforms and the intermediate domains of the African-Eurasian convergent plate boundary zone. Palaeogeography, Palaeoclimatology, Palaeoecology, 196(1–2), 209–228. https://doi.org/10.1016/S0031-0182(03)00319-5

Milly, P. C. D., & Dunne, K. A. (1994). Sensitivity of the Global Water Cycle to the Water-Holding Capacity of Land. Journal of Climate, 7(4), 506–526. https://doi.org/10.1175/1520-0442(1994)007<0506:SOTGWC>2.0.CO;2

Milly, P.C.D., and Dunne, K.A. (2016). Potential evapotranspiration and continental drying. Nature Climate Change, 6(10), 946-949. https://doi.org/10.1038/nclimate3046.

Miralles, D. G., Holmes, T. R. H., De Jeu, R. A. M., Gash, J. H., Meesters, A. G. C. A., and Dolman, A. J. (2011), Global land-surface evaporation estimates from satellite-based observations, Hydrology and Earth System Sciences, 15, 453-469, https://doi.org/10.5194/hess-15-453-2011

Mix, H. T., Mulch, A., Kent-Corson, M. L., & Chamberlain, C. P. (2011). Cenozoic migration of topography in the North American Cordillera. Geology, 39(1), 87–90. https://doi.org/10.1130/G31450.1

Mudelsee, M., & Raymo, M. E. (2005). Slow dynamics of the Northern Hemisphere glaciation. Paleoceanography, 20(4). https://doi.org/10.1029/2005PA001153

Nagavciuc, V., Scholz, P., & Ionita, M. (2022). Hotspots for warm and dry summers in Romania. Natural Hazards and Earth System Sciences, 22(4), 1347–1369. https://doi.org/10.5194/nhess-22-1347-2022

Nooni, I. K., Hagan, D. F. T., Wang, G., Ullah, W., Lu, J., Li, S., Dzakpasu, M., Prempeh, N. A., & Sian, K. T. C. L. K. (2021). Future changes in simulated evapotranspiration across continental Africa based on CMIP6 CNRM-CM6. International Journal of Environmental Research and Public Health, 18(13), 1–17. https://doi.org/10.3390/ijerph18136760

Numaguti, A. (1999). Origin and recycling processes of precipitating water over the Eurasian continent: Experiments using an atmospheric general circulation model. *Journal of* Geophysical Research Atmospheres, 104(D2), 1957–1972. https://doi.org/10.1029/1998JD200026

O'Leary, M. H. (1988). Carbon Isotopes in Photosynthesis. *BioScience*, *38*(5), 328–336. https://doi.org/10.2307/1310735

Pendergrass, A. G., & Hartmann, D. L. (2014). The Atmospheric Energy Constraint on Global-Mean Precipitation Change. Journal of Climate, 27(2), 757–768. https://doi.org/10.1175/JCLI-D-13-00163.1

Piao, S., Friedlingstein, P., Ciais, P., de Noblet-Ducoudre, N., Labat, D., & Zaehle, S. (2007). Changes in climate and land use have a larger direct impact than rising CO. PNAS, 104(39), 1–6. https://doi.org/10.1073pnas.0707213104

Poage, M. A., & Chamberlain, C. P. (2001). Empirical Relationships Between Elevation and the Stable Isotope Composition of Precipitation and Surface Waters: Considerations for Studies of Paleoelevation Change. American Journal of Science, 301(1), 1 LP – 15. https://doi.org/10.2475/ajs.301.1.1

Popov, S. V., Shcherba, I. G., Ilyina, L. B., Nevesskaya, L. A., Paramonova, N. P., Khondkarian, S. O., & Magyar, I. (2006). Late Miocene to Pliocene palaeogeography of the Paratethys and its relation to the Mediterranean. Palaeogeography, Palaeoclimatology, Palaeoecology, 238(1–4), 91–106. https://doi.org/10.1016/j.palaeo.2006.03.020

Popov, S. V., Antipov, M. P., Zastrozhnov, A. S., Kurina, E. E., & Pinchuk, T. N. (2010). Sea-level fluctuations on the northern shelf of the Eastern Paratethys in the Oligocene-Neogene. Stratigraphy and Geological Correlation, 18(2), 200–224. https://doi.org/10.1134/S0869593810020073

Raich, J. W., & Schlesinger, W. H. (1992). The global carbon dioxide flux in soil respiration and its relationship to vegetation and climate. Tellus, Series B, 44 *B*(2), 81–99. https://doi.org/10.3402/tellusb.v44i2.15428

Ring, S. J., Bocherens, H., Wings, O., & Rabi, M. (2020). Divergent mammalian body size in a stable Eocene greenhouse climate. Scientific Reports, 10(1), 1–10. https://doi.org/10.1038/s41598-020-60379-7

Rögl, F. (1999). Mediterranean and paratethys. Facts and hypotheses of an Oligocene to Miocene Paleogeography (short overview). Geologica Carpathica, 50(4), 339–349.

Rohrmann, A., Kapp, P., Carrapa, B., Reiners, P. W., Guynn, J., Ding, L., & Heizler, M. (2012). Thermochronologic evidence for plateau formation in central Tibet: By 45 Ma. Geology, 40(2), 187–190. https://doi.org/10.1130/G32530.1

Rolph, G., Stein, A., and Stunder, B., (2017). Real-time Environmental Applications and Display sYstem: READY. Environmental Modelling & Software, 95, 210-228, https://doi.org/10.1016/j.envsoft.2017.06.025

Rowley, D. B., Pierrehumbert, R. T., & Currie, B. S. (2001). A new approach to stable isotope-based paleoaltimetry: Implications for paleoaltimetry and paleohypsometry of the High

Himalaya since the late Miocene. Earth and Planetary Science Letters, 188(1–2), 253–268. https://doi.org/10.1016/S0012-821X(01)00324-7

Rowley, D.B., & Currie, B.S. (2006). Palaeo-altimetry of the late Eocene to Miocene Lunpola basin, central Tibet. Nature, 439, 677-681.

Rowley, D. B., & Garzione, C. N. (2007). Stable Isotope-Based Paleoaltimetry. Annual Review of Earth and Planetary Sciences, 35(1), 463–508. https://doi.org/10.1146/annurev.earth.35.031306.140155

Rozanski, K., Araguãs-Araguãs, L., & Gonfiantini, R. (1992). Relation between long-term trends of oxygen-18 isotope composition of precipitation and climate. Science, 258(5084), 981–985. https://doi.org/10.1126/science.258.5084.981

Rozanski, K., Araguás-Araguás, L., & Gonfiantini, R. (1993). Isotopic patterns in modern global precipitation. Washington DC American Geophysical Union Geophysical Monograph Series, 78, 1–36. https://doi.org/10.1029/GM078p0001

Rugenstein, J. K.C., & Chamberlain, C. P. (2018). The evolution of hydroclimate in Asia over the Cenozoic: A stable-isotope perspective. Earth-Science Reviews, 185, 1129–1156. https://doi.org/10.1016/j.earscirev.2018.09.003

Ruggieri, E., Herbert, T., Lawrence, K. T., & Lawrence, C. E. (2009). Change point method for detecting regime shifts in paleoclimatic time series: Application to $\delta^{18}O$ time series of the Plio-Pleistocene. Paleoceanography, 24(1), 1–15. https://doi.org/10.1029/2007PA001568

Ruprecht, E., Schröder, S. S., & Ubl, S. (2002). On the relation between NAO and water vapour transport towards Europe. Meteorologische Zeitschrift, 11(6), 395–401. https://doi.org/10.1127/0941-2948/2002/0011-0395

San Jose, M., Caves Rugenstein, J. K., Cosentino, D., Faccenna, C., Fellin, M. G., Ghinassi, M., & Martini, I. (2020). Stable isotope evidence for rapid uplift of the central Apennines since the late Pliocene. Earth and Planetary Science Letters, 544, 116376. https://doi.org/10.1016/j.epsl.2020.116376

Scheff, J., & Frierson, D. M. W. (2014). Scaling potential evapotranspiration with greenhouse warming. Journal of Climate, 27(4), 1539–1558. https://doi.org/10.1175/JCLI-D-13-00233.1

Scheff, J., Seager, R., Liu, H., & Coats, S. (2017). Are glacials dry? Consequences for paleoclimatology and for greenhouse warming. Journal of Climate, 30(17), 6593–6609. https://doi.org/10.1175/JCLI-D-16-0854.1

Schlesinger, W. H., & Jasechko, S. (2014). Transpiration in the global water cycle. Agricultural and Forest Meteorology, 189–190, 115–117. https://doi.org/10.1016/j.agrformet.2014.01.011

Schneider, U., Becker, A., Finger, P., Meyer-Christoffer, A., Ziese, M., (2018): GPCC Full Data Monthly Product Version 2018 at 0.25°: Monthly Land-Surface Precipitation from Rain-Gauges built on GTS-based and Historical Data. https://doi.org/10.5676/DWD_GPCC/FD_M_V2018_025

Seager, R., Naik, N., and Vecchi, G.A. (2010). Thermodynamic and dynamic mechanisms for large-scale changes in the hydrological cycle in response to global warming. Journal of Climate, 23(17), 4651-4668. https://doi.org/10.1175/2010JCLI3655.1

Shevenell, A. E., Kennett, J. P., & Lea, D. W. (2008). Middle Miocene ice sheet dynamics, deep-sea temperatures, and carbon cycling: A Southern Ocean perspective. Geochemistry, Geophysics, Geosystems, 9(2). https://doi.org/10.1029/2007GC001736

Simon, D., Palcu, D., Meijer, P., & Krijgsman, W. (2019). The sensitivity of middle Miocene paleoenvironments to changing marine gateways in Central Europe. Geology, 47(1), 35–38. https://doi.org/10.1130/G45698.1

Sjostrom, D. J., & Welker, J. M. (2009). The influence of air mass source on the seasonal isotopic composition of precipitation, eastern USA. Journal of Geochemical Exploration, 102(3), 103–112. https://doi.org/10.1016/j.gexplo.2009.03.001

Skinner, C. B., Poulsen, C. J., & Mankin, J. S. (2018). Amplification of heat extremes by plant CO2 physiological forcing. Nature Communications, 9(1), 1–12. https://doi.org/10.1038/s41467-018-03472-w

Sodemann, H., & Zubler, E. (2010). Seasonal and inter-annual variability of the moisture sources for alpine precipitation during 1995-2002. International Journal of Climatology, 30(7), 947–961. https://doi.org/10.1002/joc.1932

Soper, D.S. (2022). Significance of the Difference between Two Slopes Calculator [Software]. Available from https://www.danielsoper.com/statcalc

Stein, A.F., Draxler, R.R, Rolph, G.D., Stunder, B.J.B., Cohen, M.D., and Ngan, F., (2015). NOAA's HYSPLIT atmospheric transport and dispersion modeling system, Bull. Amer. Meteor. Soc., 96, 2059-2077, http://dx.doi.org/10.1175/BAMS-D-14-00110.1

Stephens, G.L. & Hu, Y. (2010). Are climate-related changes to the character of global-mean precipitation predictable? Environmental Research Letters, 5(2). https://doi.org/10.1088/1748-9326/5/2/025209.

Still, C. J., Berry, J. A., Collatz, G. J., & DeFries, R. S. (2003). Global distribution of C3 and C4 vegetation: Carbon cycle implications. Global Biogeochemical Cycles, 17(1). https://doi.org/10.1029/2001gb001807

Sun, J., Ye, J., Wu, W., Ni, X., Bi, S., Zhang, Z., Liu, W., & Meng, J. (2010). Late Oligocene-Miocene mid-latitude aridification and wind patterns in the Asian interior. Geology, 38(6), 515–518. https://doi.org/10.1130/G30776.1

Super, J. R., Thomas, E., Pagani, M., Huber, M., O'Brien, C., & Hull, P. M. (2018). North Atlantic temperature and pCO_2 coupling in the early-middle Miocene. Geology, 46(6), 519–522. https://doi.org/10.1130/G40228.1

Swann, A. L. S., Hoffman, F. M., Koven, C. D., & Randerson, J. T. (2016). Plant responses to increasing CO_2 reduce estimates of climate impacts on drought severity. Proceedings of the National Academy of Sciences of the United States of America, 113(36), 10019–10024. https://doi.org/10.1073/pnas.1604581113

Tang, Z. H., & Ding, Z. L. (2013). A palynological insight into the Miocene aridification in the Eurasian interior. Palaeoworld, 22(3–4), 77–85. https://doi.org/10.1016/j.palwor.2013.05.001

Tsanis, I., & Tapoglou, E. (2019). Winter North Atlantic Oscillation impact on European precipitation and drought under climate change. *Theoretical and Applied Climatology*, *135*(1–2), 323–330. https://doi.org/10.1007/s00704-018-2379-7

Utescher, T., Bondarenko, O. V., & Mosbrugger, V. (2015). The Cenozoic Cooling - continental signals from the Atlantic and Pacific side of Eurasia. Earth and Planetary Science Letters, 415, 121–133. https://doi.org/10.1016/j.epsl.2015.01.019

Vahmani, P., Jones, A. D., & Li, D. (2022). Will Anthropogenic Warming Increase Evapotranspiration? Examining Irrigation Water Demand Implications of Climate Change in California. Earth's Future, 10(1), 1–13. https://doi.org/10.1029/2021EF002221

van der Ent, R. J., Savenije, H. H. G., Schaefli, B., & Steele-Dunne, S. C. (2010). Origin and fate of atmospheric moisture over continents. Water Resources Research, 46(9), 1–12. https://doi.org/10.1029/2010WR009127

van der Ent, R. J., Tuinenburg, O. A., Knoche, H. R., Kunstmann, H., & Savenije, H. H. G. (2013). Should we use a simple or complex model for moisture recycling and atmospheric moisture tracking? Hydrology and Earth System Sciences, 17(12), 4869–4884. https://doi.org/10.5194/hess-17-4869-2013

van Dijk, J., Fernandez, A., Bernasconi, S. M., Caves Rugenstein, J. K., Passey, S. R., & White, T. (2020). Spatial pattern of super-greenhouse warmth controlled by elevated specific humidity. Nature Geoscience, 13(11), 739–744. https://doi.org/10.1038/s41561-020-00648-2

Varlam, C., Duliu, O. G., Ionete, R. E., & Costinel, D. (2020). Time series analysis of the $\delta^{2}H$, $\delta^{18}O$ and d-excess values in correlation with monthly temperature, relative humidity and precipitation in Râmnicu Vâlcea, Romania: 2012–2018. Geological Society Special Publication, 507(1), 77–89. https://doi.org/10.1144/SP507-2020-56

Verducci, M., Foresi, L. M., Scott, G. H., Sprovieri, M., Lirer, F., & Pelosi, N. (2009). The Middle Miocene climatic transition in the Southern Ocean: Evidence of paleoclimatic and hydrographic changes at Kerguelen plateau from planktonic foraminifers and stable isotopes. Palaeogeography, Palaeoclimatology, Palaeoecology, 280(3–4), 371–386. https://doi.org/10.1016/j.palaeo.2009.06.024

Wang, C., Dai, J., Zhao, X., Li, Y., Graham, S. A., He, D., Ran, B., & Meng, J. (2014a). Outward-growth of the Tibetan Plateau during the Cenozoic: A review. Tectonophysics, 621, 1–43. https://doi.org/10.1016/j.tecto.2014.01.036

Wang, L., Good, S. P., & Caylor, K. K. (2014b). Global synthesis of vegetation control on evapotranspiration partitioning. Geophysical Research Letters, 41, 6753–6757. https://doi.org/10.1002/2014GL061439.Received

Wang, S., Zhang, M., Crawford, J., Hughes, C. E., Du, M., & Liu, X. (2017). The effect of moisture source and synoptic conditions on precipitation isotopes in arid central Asia. Journal of Geophysical Research, 122(5), 2667–2682. https://doi.org/10.1002/2015JD024626

Waterisotopes Database (2020) http://waterisotopes.org. Accessed 12/1/2020.

Wei, Z., Yoshimura, K., Wang, L., Miralles, D. G., Jasechko, S., & Lee, X. (2017). Revisiting the contribution of transpiration to global terrestrial evapotranspiration. Geophysical Research Letters, 44(6), 2792–2801. https://doi.org/10.1002/2016GL072235

White, W. B. (2019). Speleothems. In Encyclopedia of Caves (3rd ed.). Elsevier Inc. https://doi.org/10.1016/b978-0-12-814124-3.00117-5

Winnick, M. J., Chamberlain, C. P., Caves, J. K., & Welker, J. M. (2014). Quantifying the isotopic "continental effect." Earth and Planetary Science Letters, 406, 123–133. https://doi.org/10.1016/j.epsl.2014.09.005

Winschall, A., Pfahl, S., Sodemann, H., & Wernli, H. (2014). Comparison of Eulerian and Lagrangian moisture source diagnostics - The flood event in eastern Europe in May 2010. Atmospheric Chemistry and Physics, 14(13), 6605–6619. https://doi.org/10.5194/acp-14-6605-2014

Woodward, F. I. (1993). Plant responses to past concentrations of carbon dioxide. Vegetatio, 104–5(145–155; 35 ref.), 145–155.

Wypych, A., Bochenek, B., & Rózycki, M. (2018). Atmospheric moisture content over Europe and the Northern Atlantic. Atmosphere, 9(1). https://doi.org/10.3390/atmos9010018

Xiangyu, L. I., Dabang, J., Zhongshi, Z., Ran, Z., Zhiping, T., & Qing, Y. A. N. (2015). Mid-Pliocene Westerlies from PlioMIP Simulations. Advances in Atmospheric Sciences, 32(July), 909–923. https://doi.org/10.1007/s00376-014-4171-7.1.

Zveryaev, I. I., Wibig, J., & Allan, R. P. (2008). Contrasting interannual variability of atmospheric moisture over Europe during cold and warm seasons. Tellus, Series A: Dynamic Meteorology and Oceanography, 60 A(1), 32–41. https://doi.org/10.1111/j.1600-0870.2007.00283.x

For references for the modern and proxy compilations, see Supplement 1 (modern Eurasian $\delta^{18}O$), Supplement 2 (Europe paleo-$\delta^{18}O$), and Rugenstein and Chamberlain, 2018 (Asia paleo-$\delta^{18}O$).

Appendix

Table A1. Averages of $\delta^{18}O$ in Europe and Asia by epoch of filtered data (<50°E: 47°- 55°N; >50°E: 35°- 55°N) **without lacustrine values**, with p-value from t-test of significant difference between the two populations within a single epoch (‰ VSMOW; slope of the longitudinal gradient: ‰/°longitude).

Geologic Epoch	Europe $\delta^{18}O$	SD	Asia $\delta^{18}O$	SD	P-value	Gradient
Modern	-9.06	1.61	-11.15	3.04	3.25e-11*	-0.023
Quaternary	-8.73	2.61	-8.73	2.22	0.99	-0.0079
Pliocene	-9.30	0.98	-8.55	1.63	0.13	0.013
Late Miocene	-5.30	0.63	-7.67	1.73	0.029*	-0.020
Early Miocene	-7.04	1.11	-8.95	1.92	0.021*	-0.018
Oligocene	-5.96	3.47	-9.10	1.83	0.039*	-0.039
Eocene	-4.31	4.16	-7.44	1.75	0.047*	-0.040

*Indicates statistical significance between Europe and Asia isotope populations ($p < 0.05$)

Table A2. Comparison of the $\delta^{18}O$ gradient (<50°E: 47°-55°N; >50°E: 35°-55°N) between neighboring epochs **without lacustrine values** using 1) confidence intervals at which the slope of the gradients are statistically distinct and 2) p-values from t-test of significant difference between preceding epochs.

Geologic Epoch	Confidence Interval at which Slopes are different	P-value
Quaternary-Pliocene	98%	0.27
Pliocene-Late Miocene	99%	0.048*
Late Miocene-Early Miocene	1%	0.93
Early Miocene-Oligocene	90%	0.96
Oligocene-Eocene	10%	0.27

*Indicates statistical significance of change in the isotope gradient between neighboring epochs ($p < 0.05$)

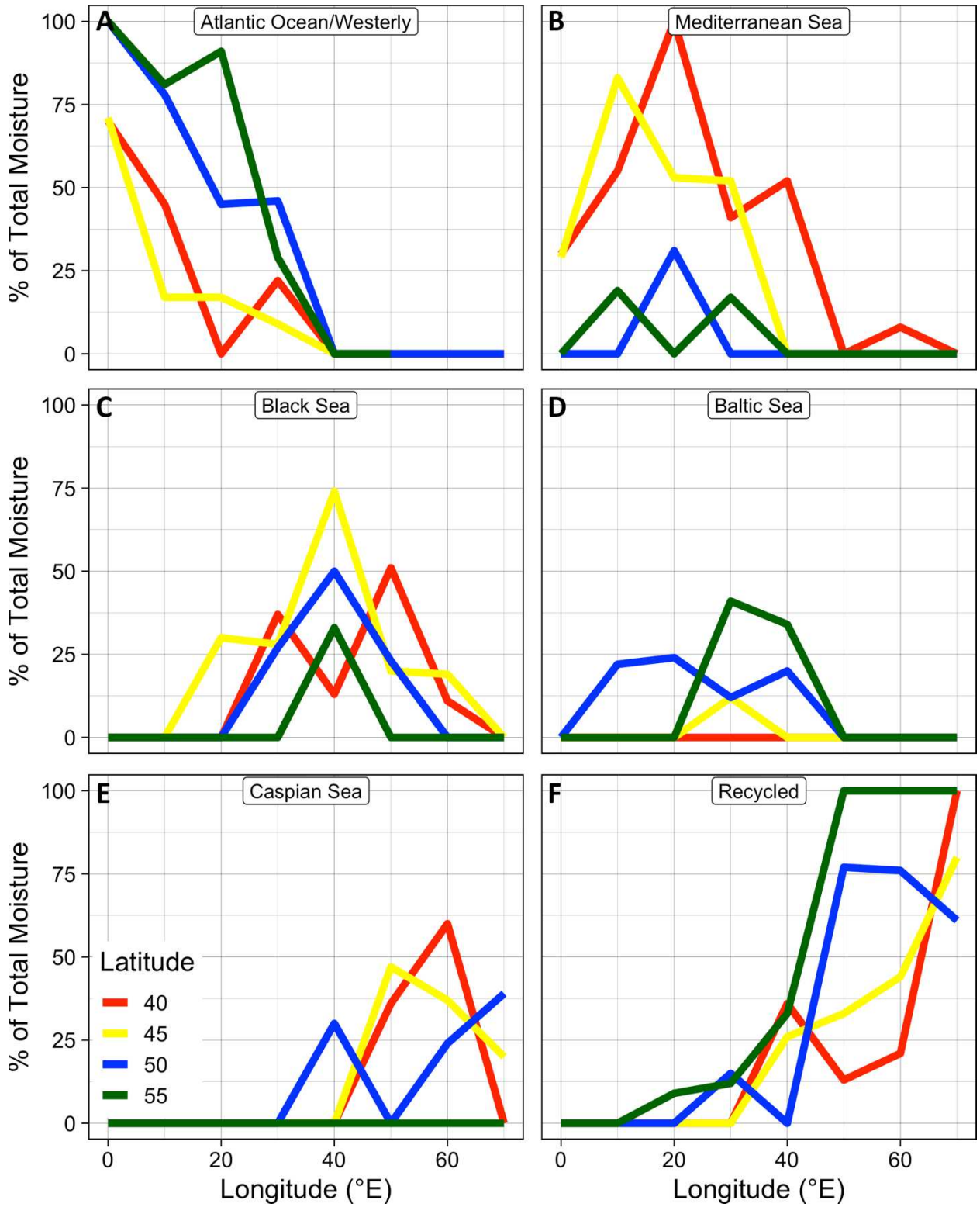

Figure A1A-F. Results from HYSPLIT modeling showing the relative contribution of six major moisture sources across Eurasia (A) Atlantic, B) Mediterranean, C) Black Sea, D) Baltic Sea, E) Caspian Sea, and F) Recycled terrestrial moisture) to a set of gridded sites. Lines are colored by latitude (40-55°N).

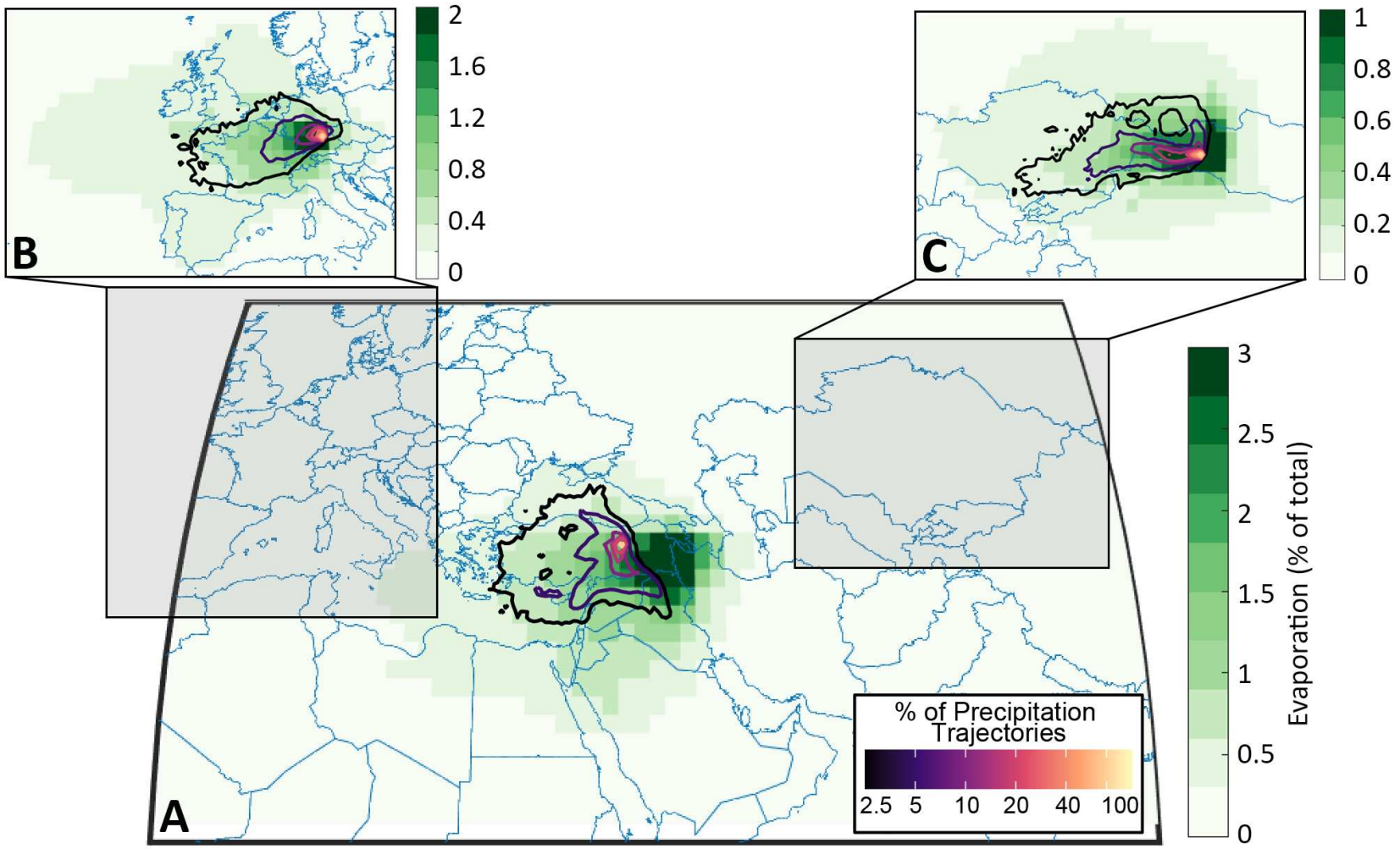

Figure A2A-C. Results from the WAM (green, gridded cells) compared with HYSPLIT results (purple-yellow density contours) from the same, or nearby, locations in Eurasia. Results demonstrate that HYSPLIT air parcel tracking roughly matches that produced by moisture backtracking from the WAM. Note the differing scales for the % of total evaporation from each location. A) Comparison of HYSPLIT results at 40N, 40E to WAM results at 40N, 45E. B) Comparison of HYSPLIT results at 50N, 10E with WAM results at the same location. C) Comparison of HYSPLIT results at 47N, 93E with WAM results at the same location.

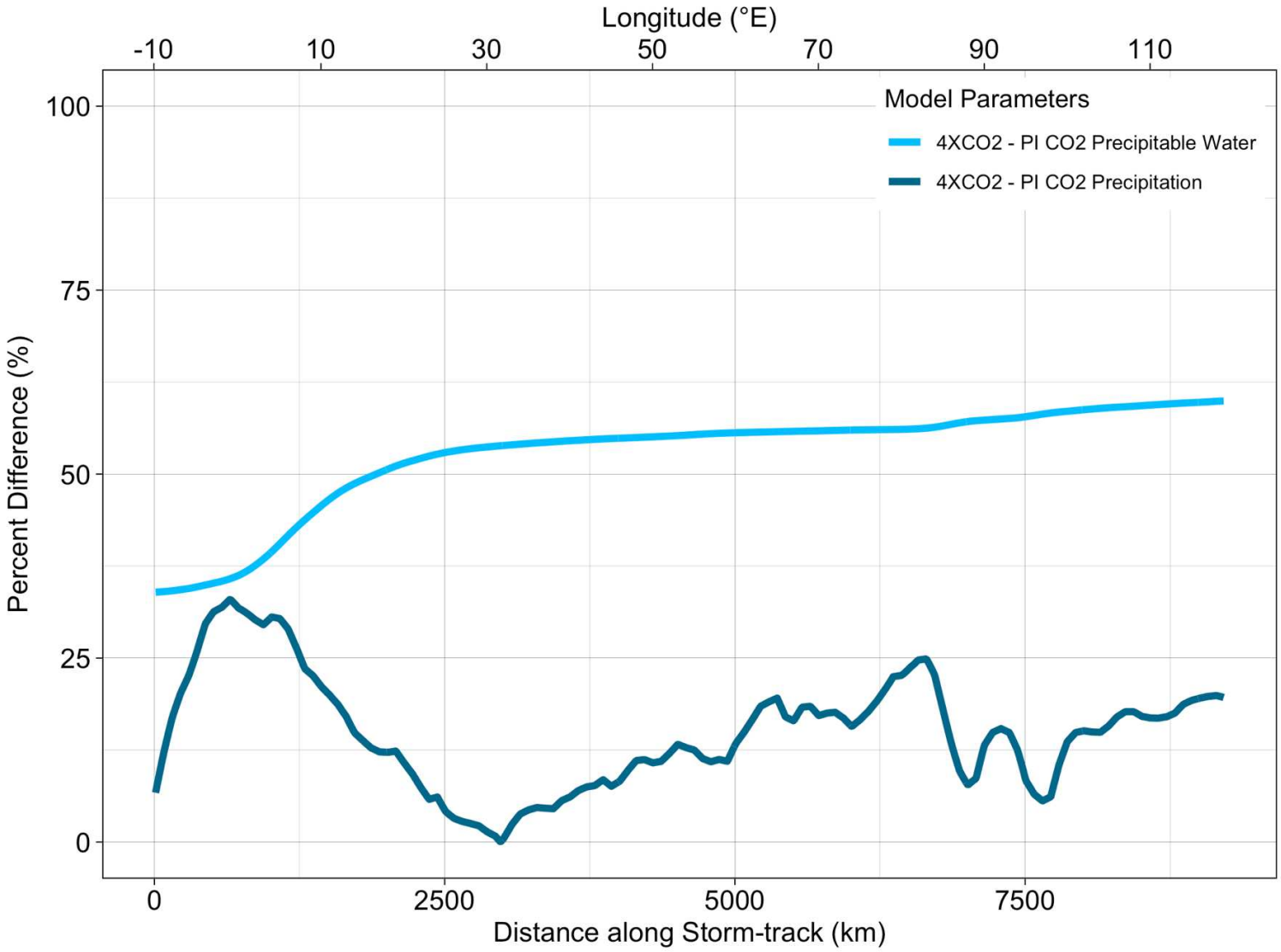

Figure A3. Plot of the percent change in precipitable water (light blue line) and precipitation (dark blue line) between CESM forced at 4xCO_2 and Pre-Industrial CO_2 concentrations run through the reactive transport model. The plot demonstrates the faster increase of PW relative to P at higher CO_2 concentrations.

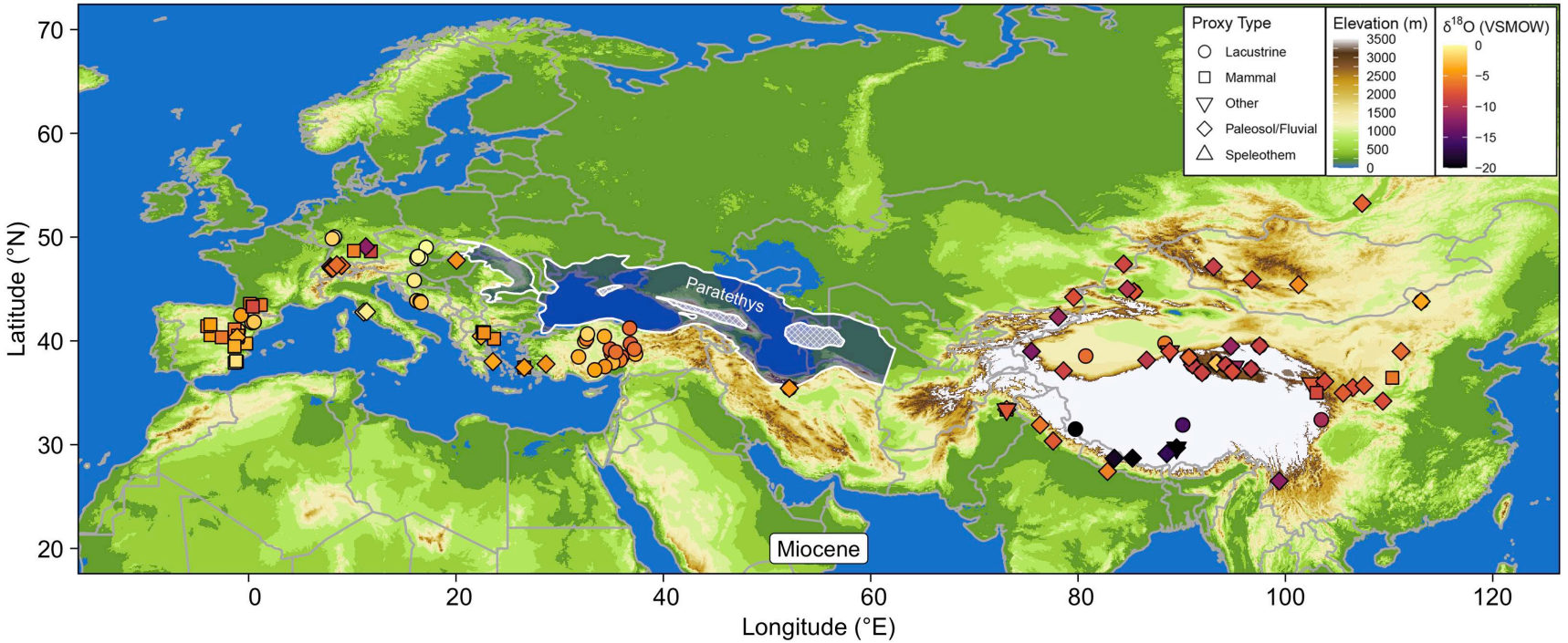

Figure A4. Map of Miocene $\delta^{18}O_w$ proxy data with mid-Miocene extent of the Paratethys. Crosshatched, shaded areas indicate islands within the Paratethys. Paratethys boundaries originally published in Popov et al. (2010) and digitized by Dr. Adam Forte.